NAVAL POSTGRADUATE SCHOOL

MONTEREY, CALIFORNIA

THESIS

DETERMINING CHANGES IN THE DYNAMIC MATERIAL RESPONSE OF BORON CARBIDE ABOVE THE HUGONIOT ELASTIC LIMIT FROM SILICON ELEMENTAL INCLUSION

by

Antonios Varvasoudis

September 2023

Thesis Advisor:	Raymond M. Gamache
Co-Advisor:	Frank A. Narducci

THIS PAGE INTENTIONALLY LEFT BLANK

REPORT DOCUMENTATION PAGE	*Form Approved OMB No. 0704-0188*

Public reporting burden for this collection of information is estimated to average 1 hour per response, including the time for reviewing instruction, searching existing data sources, gathering and maintaining the data needed, and completing and reviewing the collection of information. Send comments regarding this burden estimate or any other aspect of this collection of information, including suggestions for reducing this burden, to Washington headquarters Services, Directorate for Information Operations and Reports, 1215 Jefferson Davis Highway, Suite 1204, Arlington, VA 22202-4302, and to the Office of Management and Budget, Paperwork Reduction Project (0704-0188) Washington, DC, 20503.

1. AGENCY USE ONLY ***(Leave blank)***	**2. REPORT DATE** September 2023	**3. REPORT TYPE AND DATES COVERED** Master's thesis

4. TITLE AND SUBTITLE DETERMINING CHANGES IN THE DYNAMIC MATERIAL RESPONSE OF BORON CARBIDE ABOVE THE HUGONIOT ELASTIC LIMIT FROM SILICON ELEMENTAL INCLUSION	**5. FUNDING NUMBERS** RPK49
6. AUTHOR(S) Antonios Varvasoudis	
7. PERFORMING ORGANIZATION NAME(S) AND ADDRESS(ES) Naval Postgraduate School Monterey, CA 93943-5000	**8. PERFORMING ORGANIZATION REPORT NUMBER**
9. SPONSORING / MONITORING AGENCY NAME(S) AND ADDRESS(ES) MarCorSysCom, Quantico, VA 22134	**10. SPONSORING / MONITORING AGENCY REPORT NUMBER**

11. SUPPLEMENTARY NOTES The views expressed in this thesis are those of the author and do not reflect the official policy or position of the Department of Defense or the U.S. Government.

12a. DISTRIBUTION / AVAILABILITY STATEMENT Approved for public release. Distribution is unlimited.	**12b. DISTRIBUTION CODE** A

13. ABSTRACT (maximum 200 words)

Boron carbide (B4C) is a well-known ceramic demonstrating excellent hardness and compressive strength while maintaining a low density (2.52 g/cm3). Despite its promising characteristics, catastrophic failure is observed for impact pressures near and above the Hugoniot elastic limit (HEL). Several publications suggest that B4C, under pressures near the HEL, eject carbon atoms enabling amorphous shear band formations leading to catastrophic failure.

Recent studies suggest that uniform placement of Si, within B4C, may support both an exothermic reaction with the ejected C forming SiC and removing the free carbon as well as replacing polar carbon sites that are ultimately believed to be the source of ejected carbon. Within this investigation, variation in stoichiometry ratios of Si, and Zr within B4C, will be investigated and correlated to the elastic precursor response both at the HEL and transitions to the shock wave.

14. SUBJECT TERMS boron carbide, B4C, silicon, Si, Hugoniot, Hugoniot elastic limit, HEL	**15. NUMBER OF PAGES** 103
	16. PRICE CODE

17. SECURITY CLASSIFICATION OF REPORT Unclassified	**18. SECURITY CLASSIFICATION OF THIS PAGE** Unclassified	**19. SECURITY CLASSIFICATION OF ABSTRACT** Unclassified	**20. LIMITATION OF ABSTRACT** UU

NSN 7540-01-280-5500

Standard Form 298 (Rev. 2-89)
Prescribed by ANSI Std. 239-18

DETERMINING CHANGES IN THE DYNAMIC MATERIAL RESPONSE OF BORON CARBIDE ABOVE THE HUGONIOT ELASTIC LIMIT FROM SILICON ELEMENTAL INCLUSION

Antonios Varvasoudis
Captain, Hellenic Air Force
BSAE, Hellenic Air Force Academy, 2008

Submitted in partial fulfillment of the
requirements for the degree of

MASTER OF SCIENCE IN APPLIED PHYSICS

from the

NAVAL POSTGRADUATE SCHOOL
September 2023

Approved by: Raymond M. Gamache
Advisor

Frank A. Narducci
Co-Advisor

Frank A. Narducci
Chair, Department of Physics

THIS PAGE INTENTIONALLY LEFT BLANK

ABSTRACT

Boron carbide (B4C) is a well-known ceramic demonstrating excellent hardness and compressive strength while maintaining a low density (2.52 g/cm3). Despite its promising characteristics, catastrophic failure is observed for impact pressures near and above the Hugoniot elastic limit (HEL). Several publications suggest that B4C, under pressures near the HEL, eject carbon atoms enabling amorphous shear band formations leading to catastrophic failure.

Recent studies suggest that uniform placement of Si, within B4C, may support both an exothermic reaction with the ejected C forming SiC and removing the free carbon as well as replacing polar carbon sites that are ultimately believed to be the source of ejected carbon. Within this investigation, variation in stoichiometry ratios of Si, and Zr within B4C, will be investigated and correlated to the elastic precursor response both at the HEL and transitions to the shock wave.

THIS PAGE INTENTIONALLY LEFT BLANK

Table of Contents

THIS PAGE INTENTIONALLY LEFT BLANK

List of Figures

List of Tables

THIS PAGE INTENTIONALLY LEFT BLANK

List of Acronyms and Abbreviations

B_4C	Boron Carbide
Cu	Copper
DFT	Density Functional Theory
DOD	Department of Defense
ESAPI	Enhanced Small Arms Protection Insert
EoS	Equation of State
EXAFS	Extended X-ray Absorption Fine Structure
FMJ	Full Metal Jacket
HEBM	High-Energy Ball Milling
HEL	Hugoniot Elastic Limit
LiF	Lithium Fluoride
NBR	Non-Back-Reflecting
NIJ	National Institute of Justice
OFHC	Oxygen Free High-Conductivity
PDV	Photon Doppler Velocimetry
SAPI	Small Arms Protection Insert
SEM	Scanning Electron Microscope
Si	Silicon
SiC	Silicon Carbide
SIRHEN	Sandia InfraRed HEterodyne aNalysis
TMD	Theoretical Maximum Density
UHMWPE	Ultra-High-Molecular-Weight Polyethylene
VOA	Variable Optical Attenuator

XRD	X-Ray Diffraction
XSAPI	Extended Performance Small Arms Protection Insert
Zr	Zirconium

Acknowledgments

Dr. Ray Gamache, you are the first person that I would like to thank for accepting me as your thesis student. Beside you, I had the opportunity to move across many disciplines, related to physics and engineering. You introduced me to the experimental process not only in the lab but also in how we can use it in daily life. You taught me things that would apply to my thesis and my car repairs (I remember all of our conversations and pieces of advice). Thank you for your patience and your kindness. Thank you for your friendship as this is also part of my experience in the U.S.

I would like also to thank Dr. Frank Narducci for serving as my co-advisor, but also for his support in my robotics certificate as he explained to me many theoretical questions that I had. I would also like to thank all NPS faculty and all my professors for the Postgraduate Degree experience. They make me feel like studying in my country without worrying any time about the language barrier.

I would also like to thank all of my classmates over these two years, for bringing me into their lives and introducing me to the U.S. culture. Their positivity and respect improved me as a person and as an officer.

Lastly but very importantly, I would like to thank my spouse Maria for her support and understanding while the nights were long and some weekends were lost. She was beside me during this long and wonderful journey at NPS and without her, this experience would not be so rich in everything. I would also like to thank my parents for being beside me these two years through many long video calls.

All of you put some bricks in my life, building my education, knowledge, trust, friendships, dignity...Thank you all for these two years!

THIS PAGE INTENTIONALLY LEFT BLANK

CHAPTER 1:
Introduction

Higher-performance anti-personnel rounds raise the demand for more advanced armor systems. New body armor materials are required to enable defeat from high-performance armor-piercing rounds while maintaining a low areal density. The defeat of armor-piercing rounds requires a front-face ceramic system capable of both blunting and reducing the velocity of the incident-hardened high-density round. The front ceramic armor should both have a higher hardness and the ability to remain intact for a duration enabling a significant deformation and velocity reduction to the incident projectile.

The most commonly used ceramics for protection levels up to National Institute of Justice (NIJ) level IV include Aluminum oxide (Al_2O_3), Silicon Carbide (SiC), and Boron Carbide (B_4C). The lightest of these three is the B_4C, with a density of approximately $2.52\, g/cm^3$. Currently, for higher-performance armor systems, such as the Extended Performance Small Arms Protection Insert (XSAPI) system, only Silicon Carbide (SiC) is integrated within the armor system as B_4C experiences a catastrophic failure and the areal density of alumina for XSAPI applications is too heavy.

Two issues exist with B_4C applied to armor systems: high manufacturing costs and premature failure for impact pressures above the Hugoniot Elastic Limit (HEL). Manufacturing B_4C ceramic plates requires simultaneous high pressure (3000 psi) and temperature (2200^o C). This process increases the cost and limits the production throughput. The second issue is the inability of B_4C to handle high-pressure impacts near and above the HEL. Under impacts near the HEL ($\sim 20\, Gpa$), carbon atoms, migrate from the icosahedron (polar location) and transfer to the 3-atom chain forming C-C-C chains that eject from the B_4C, enabling amorphous graphite to form within shear bands leading to catastrophic failure. This catastrophic failure for impact pressures above the HEL prevents the use of B_4C in high-performance armor systems.

This thesis investigates if elemental inclusions placed within B_4C can prevent amorphous shear band failure. Materials placed within B_4C include both Silicon (Si) and Zirconium (Zr). Si, modeled within Density Functional Theory (DFT), is shown to improve the toughness of pure B_4C by altering the icosahedron structure and possibly preventing the release of carbon atoms forming amorphous shear bands. Both Si and Zr enable an exothermic reaction when introduced to free carbon under elevated temperatures and pressures. The exothermic reaction supports both the removal of free carbon as well as an increase in internal pressure from the exothermic reaction. Zr has a higher exothermic reaction as compared to Si.

High-Energy Ball Milling (HEBM) can be used to place elemental inclusions within the B_4C unit cell. The HEBM process enables both the reduction in grain size of B_4C and the elemental inclusion of Si and Zr into the B_4C lattice. The energy provided by HEBM enables the placement of studied elements within the unit cell of B_4C.

After the raw material preparation, being in a powder form, the powder is hot pressed into disks under a high temperature of 2200 ^{o}C and pressure of 3000 psi. The disks are Blanchard ground to ensure parallelism for shock impact experiments. Within the thesis, there are five different ceramic materials studied: (1) B_4C "as bought," (2) HEBM B_4C, (3) HEBM B_4C $/\frac{1}{2}$ Si atom (per unit cell), (4) HEBM B_4C $/1$ Si atom (per unit cell) and (5) HEBM B_4C $/1$ Zr atom (per unit cell).

Powder samples are analyzed through X-Ray Diffraction (XRD) and Scanning Electron Microscope (SEM). Once the powder samples are quantified, the powder is hot pressed and Blanchard ground to 34mm x 5mm discs to enable shock impact studies. All impact studies use a single-stage 40mm powder gun achieving an impact velocity of ~2.0 km/s. To determine the impact conditions, the impact velocity/orientation, and the impact interface particle velocity are measured.

Each impact enables pressures above the HEL. As the B_4C reaches the HEL, the samples are studied to see if the material experiences the amorphous shear band failure through the elastic precursor wave response to the impact pressure above the HEL. Based on the transition from elastic to the shock wave, the effects of both HEBM and elemental inclusions are studied and documented.

CHAPTER 2:
Problem Assessment

2.1 Body Armor Systems

Body armor systems are designed to defeat defined threats (e.g., rifled bullets). Their typical structure consists of a front ceramic face backed by a high-tensile strength textile material. Based on the identified threat, variations in the ceramic type/thickness and type/thickness of the textile backing are engineered to enable the defeat of the identified threat.

Textile backing systems, used for armor, have a high mass efficiency provided the incident projectiles are below a certain impact pressure limit. Under high impact pressures, the textile backing system provides minimal penetration resistance [1]. The purpose of the front ceramic plate is to both blunt and reduce the impact velocity and ultimately reduce the incident pressure on the textile backing system. In other words, the ceramic does not have to arrest it but simply preconditions the incident projectile to engage the textile layer to arrest the incoming projectile [2], [3].

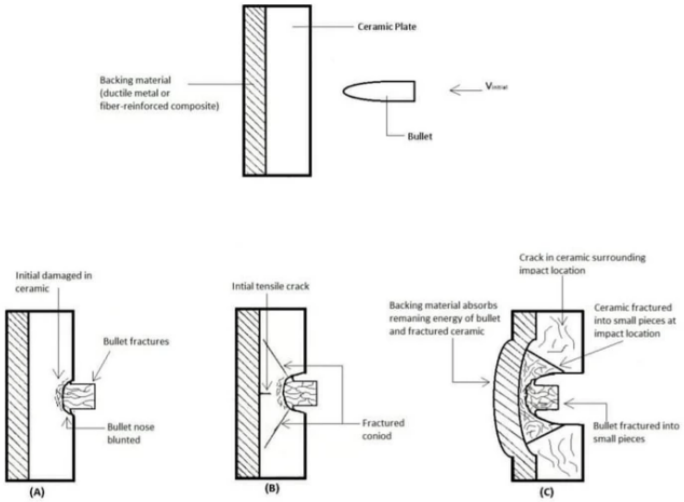

Figure 2.1. Projectile Impact Phases

Current textiles used in armor applications are typically aramid fibers (Kevlar) and Ultra-High-Molecular-Weight Polyethylene (UHMWPE). The latter, in overall comparison, greatly exceeds Kevlar's performance in both material strength and hydrophobic properties. UHMWPE is fabricated by applying repeated 4 layers of 0^o and 90^o filament orientation followed by a heated pressing at 250^o C and 3000 – 5000 psi, (figure 2.2a). In pressed form, the UHMWPE exhibits a high performance but remains rigid. Kevlar exhibits a reduced performance but remains more compliant. UHMWPE can be applied in a flexible unpressed form, but the performance is reduced.

Most current body armor systems incorporate UHMWPE as the backing system. The design of the body armor system includes addressing the performance of the composite armor, including both the ceramic and the textile components. Ideally, front-face ceramic systems should be designed to a thickness that enables the reduction in pressure to arrest the threat projectile with the textile backing system. As the threat performance is increased, both the front ceramic plate and the textile backing thickness are increased [1], [4].

(a) (b)

Figure 2.2. (a) UHMWPE Textile Armor Backing Plate (b) ESAPI Armor Plate

Two widely known plates that are currently used by the Department of Defense (DOD) to provide protection in combat environments include the Small Arms Protection Insert (SAPI) and the Enhanced Small Arms Protection Insert (ESAPI). The former one may defeat NIJ level III threats which are similar to a 7.62 mm Full Metal Jacket (FMJ) lead core ammunition

(M80). The latter one was manufactured as an improvement to SAPI, and it can provide protection up to NIJ level IV [5].

Both SAPI and ESAPI body armor systems use a ceramic front face system primarily incorporating either SiC or B_4C with an UHMWPE textile backing system. A requirement to defeat higher threats defined the next level of body armor within the XSAPI plates. Within the higher-threat projectiles, it was found that only SiC was able to defeat the identified threat. During the application using B_4C, catastrophic failure occurs when the threat impact pressure is close to the HEL, Figure 2.3 [6], [7].

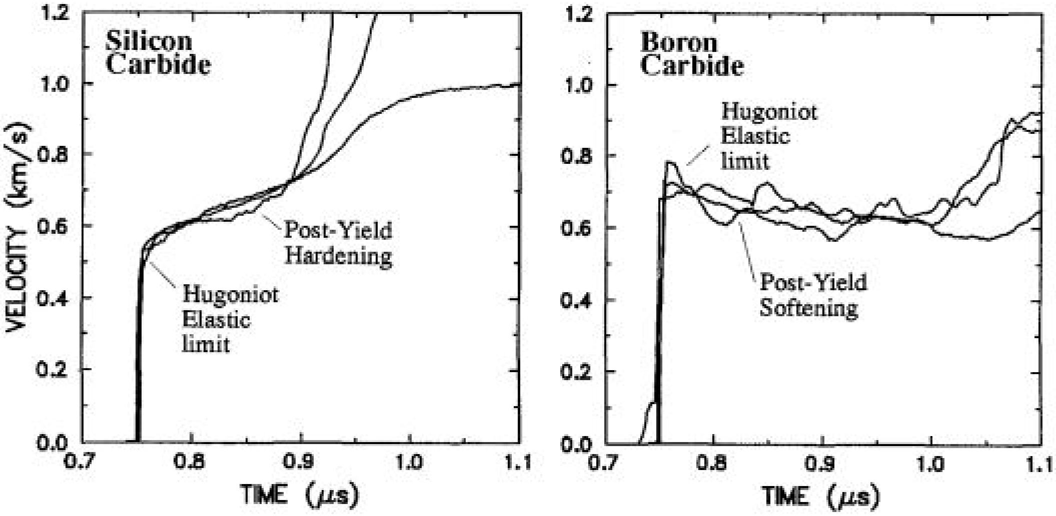

Figure 2.3. Impact Response of SiC (left) vs. B_4C (right). Source: [7].

Under this pressure load within B_4C, exceeding the elastic limit ($\sim 18\,GPa$), carbon atoms are ejected from the unit cell and form within shear bands. As mentioned previously, impact pressures within B_4C, near the HEL, enable catastrophic failure [7]. This deficiency prevents the use of B_4C in XSAPI body armor systems as impact threats exceed the HEL. SiC can be applied as the front face ceramic, but there is a weight penalty.

This thesis investigates chemical alterations to B_4C, which could enable the prevention of amorphous shear band failure. The ability to use B_4C within the XSAPI system will enable a reduction in areal density by 21.4%.

2.2 Boron Carbide Structure

B_4C has a rhombohedral crystallographic lattice, with a unit cell consisting of an icosahedron structure linked through a three-atom chain forming the unit cell, Figure 2.4 [8].

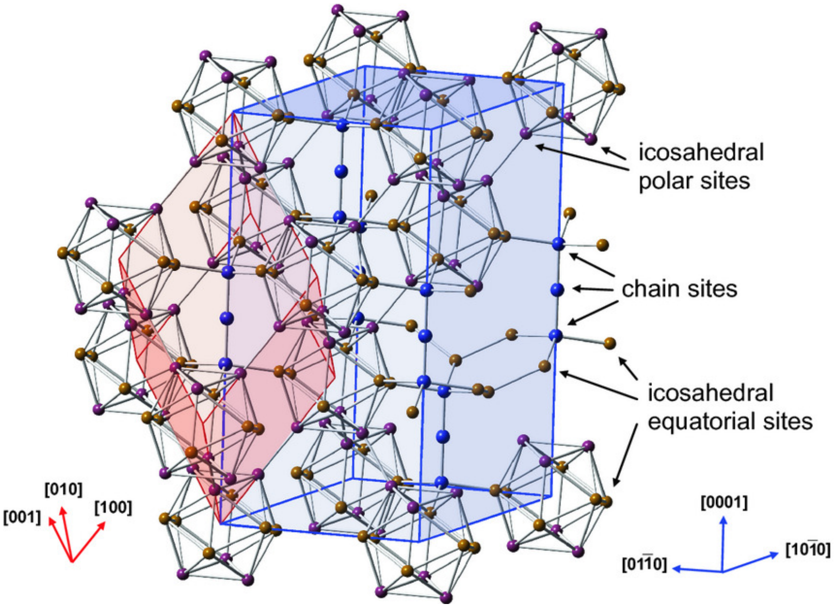

Figure 2.4. B_4C Lattice. Source: [8].

While the nominal status of B_4C has twelve atoms of boron in the icosahedron and three carbon atoms at the chain, DFT reveals at least six prototypes, which differ in B and C composition and location. Possible location types are the polar and equatorial sites. The polar sites correspond to the linking positions of the icosahedrons, while the equatorial ones are the chain connection points (Figure 2.4). The three most common polytypes are B_4C, $B_{11}C^P$-CBC, $B_{12}C$-CCC and $B_{12}C$-CBC with $B_{11}C^P$-CBC constituting over 90% by weight. (p superscript corresponds to the polar site of the carbon location) [8], [9].

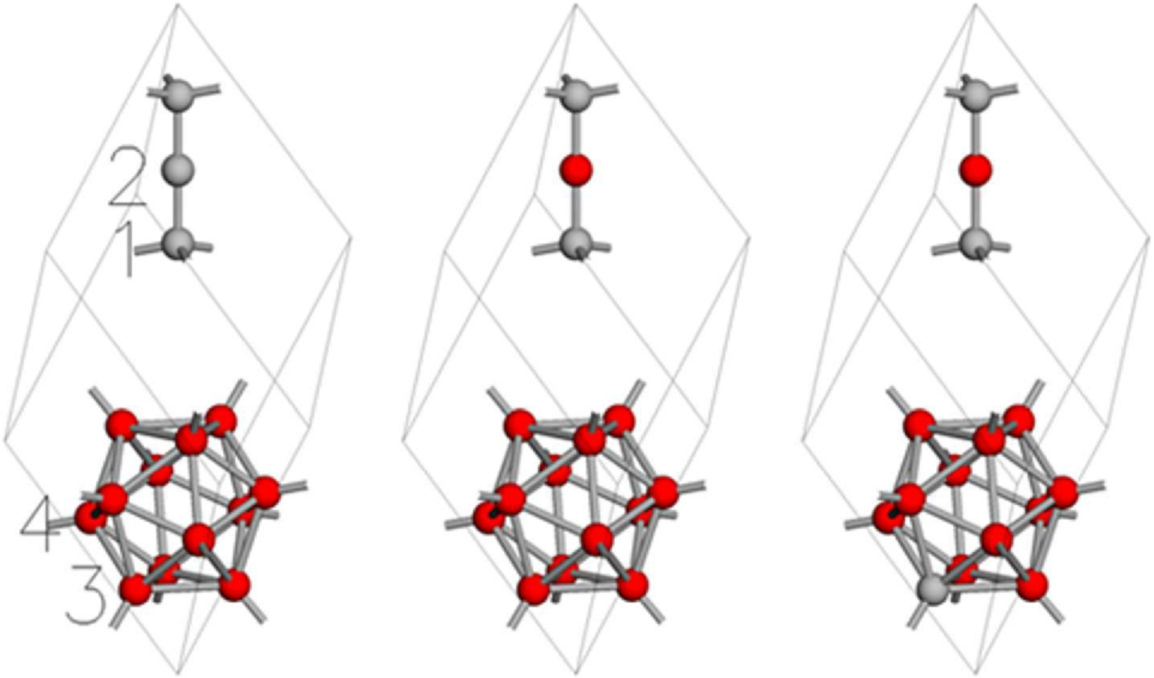

Figure 2.5. B_4C Primitive Cells from left to right $B_{12}C^P$-CCC, $B_{12}C^P$-CBC and $B_{11}C^P$-CBC, B (red spheres) and C (grey spheres). Source: [8].

$B_{11}C^P$-CBC is the preferred unit cell with the lowest energy of formation [9]. Four types of bonding exist in the B_4C structure:

1. the intrachain, connecting the chain end atom,
2. the chain-icosahedron between the chain and equatorial site,
3. the intericosahedral, polar site, and
4. the intraicosahedral, equilateral site

Studies utilizing XRD showed that the intrachain bond length is the smallest, followed by the chain-icosahedron, the intericosahedral, and finally, the intraicosahedral bond length. As the bond length is inversely related to stiffness, the intra-chain bond is the most rigid in B_4C [9].

Further studies [10], [11] argued that the central atom in the chain could move in a plane normal to the bond axis, preserving a force for atomic displacement in the chain's direction. The bond softness was determined by Raman spectra of B_4C, connecting a specific band with the chain bonds related to the rotation of the central chain atom. As a result, B_4C presents an anisotropy on its stiffness according to the principal directions of the rhombohedral lattice. It is implied that deformation under specific vectors leads to bond rotation instead of contraction, which alters the B_4C behavior under impacts near HEL. In other words, the central boron atom within the chain center can bond with neighboring atoms in other icosahedrons, leading to energetically preferred structures, the collapse of B_4C structure, and the formation of amorphized shear bands.

During uniaxial compression, above the HEL of B_4C ($>\sim 20\,GPa$) [12], material surface relief cracks and shear bands are optically noticeable during the unloading. Observations suggest that once the HEL is exceeded, B_4C softens [7], [13]–[16], unlike other ceramics like SiC which hardens, leading to lower energy dissipation. This glass-liked behavior relates to the above amorphous shear band formation along specific planes, localizing strains and leading to material softening [8]. Many different explanations have been given for the failure caused by the formation of amorphous shear bands. Some of them are related to the bending of the interconnection chain. Others referred to either a crosslinking or a breakup structure of icosahedra [9], [17].

Specifically, the most favored transformation of $B_{11}C^P$-CBC from an energy perspective, is the decomposition into B_{12} icosahedra and graphite CCC [18]. During this decomposition, it is proposed migration of carbon from the polar to the equatorial and then to the chain center position. Simultaneously the boron atom moves into the icosahedron polar site. It is predicted that the CCC chain requires a low pressure to separate for the unit cell, and the free carbon relocates to within identified shear bands [9].

Altering chemical bonds within B_4C could prevent the migration of the polar carbon atoms supporting the CCC chain formation within the $B_{11}C^P$-CBC polytype under high-impact loads. Through the elemental inclusion of various elements into the B_4C lattice, the energy to move the polar carbon out of the icosahedron may be increased [8]. DFT calculates the preferred locations of different elements if placed within the B_4C unit cell. Within the calculations, for the $B_{11}C^P$-CBC polytype, metals prefer the center chain site while non-metals prefer the chain end positions, and semi-metals show preference to the icosahedron polar site. Because $B_{11}C^P$-CBC is the most common polytype, the elemental substitution position for each identified element gives the most probable positions for them [8]. Specifically, in a study based on Si inclusion, DFT showed that Si prefers the center position in the chain of $B_{12}C$-CCC and $B_{12}C$-CBC polytypes of B_4C, while the polar position is more favored for the polytype $B_{11}C^P$-CBC, shown in the Figure 2.6 [8]. Such an elemental inclusion can replace the polar carbon atom with Si as they both have the same preferred position. If the Si is able to be placed within the polar sight, it could prevent the migration of boron from the center chain position into the icosahedron enabling the formation of amorphous graphite bands.

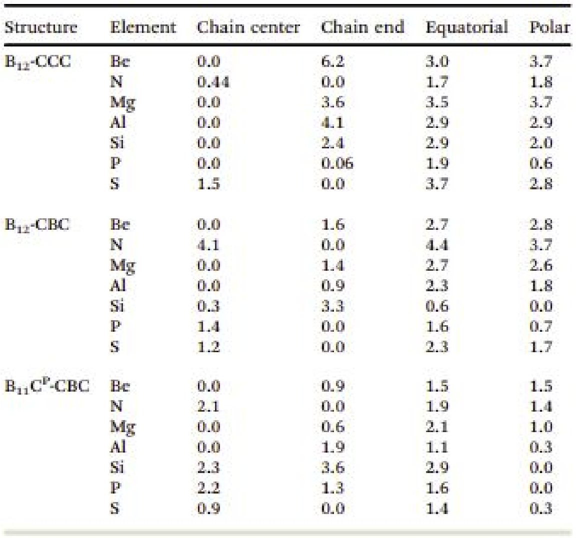

Structure	Element	Chain center	Chain end	Equatorial	Polar
B_{12}-CCC	Be	0.0	6.2	3.0	3.7
	N	0.44	0.0	1.7	1.8
	Mg	0.0	3.6	3.5	3.7
	Al	0.0	4.1	2.9	2.9
	Si	0.0	2.4	2.9	2.0
	P	0.0	0.06	1.9	0.6
	S	1.5	0.0	3.7	2.8
B_{12}-CBC	Be	0.0	1.6	2.7	2.8
	N	4.1	0.0	4.4	3.7
	Mg	0.0	1.4	2.7	2.6
	Al	0.0	0.9	2.3	1.8
	Si	0.3	3.3	0.6	0.0
	P	1.4	0.0	1.6	0.7
	S	1.2	0.0	2.3	1.7
$B_{11}C^P$-CBC	Be	0.0	0.9	1.5	1.5
	N	2.1	0.0	1.9	1.4
	Mg	0.0	0.6	2.1	1.0
	Al	0.0	1.9	1.1	0.3
	Si	2.3	3.6	2.9	0.0
	P	2.2	1.3	1.6	0.0
	S	0.9	0.0	1.4	0.3

Figure 2.6. Relative Energy in eV for Substitutional Elements in B_4C Prototypes' Lattice. Source: [8].

In addition to locating the Si atom within the polar site, the Si may also locate within interstitial positions. By locating the Si atom within interstitial positions, the Si atom could react with free carbon atoms forming SiC. This reaction is both exothermic energy and can reduce the free carbon within the amorphous shear band. Both mechanisms could prevent the release of free carbon [8].

A second study is performed using Zr while its reaction with carbon provides a higher exothermic reaction. No study was performed as to the theoretical locations of Zr within the B_4C, but the key interest is the change in performance caused by an element providing a much larger exothermic reaction with the carbon. The objective is to study the elemental inclusion of both Si and Zr within B_4C as well as the ability to prevent the currently observed amorphous shear band failure [19], [20].

CHAPTER 3:
Experimental Process

3.1 Ceramic Target Preparation

3.1.1 High-Energy Ball Milling

There are limited techniques to enable Si inclusion within the B_4C lattice. Elemental inclusion within B_4C requires temperatures above 1100 ^oC under atmospheric conditions that cause instability to the B_4C lattice and carbon diffusion from the B_4C lattice. Sintering techniques within B_4C to produce alloys require temperatures of approximately 1500 ^oC to enable elements to integrate within the B_4C unit cell. So at these temperatures, the original lattice structure is not retained. Rather the diffused carbon would form separate phases. For example, in Si alloys, the separate phase would consist of SiC [8].

One known technique that provides the energies to enable the placement of elements within the B_4C unit cell, while avoiding carbon diffusion, is HEBM [21]. Through HEBM, kinetic energy can be imparted into the powder of interest through collisions between the powder, grinding media spheres, and the ball-milling container walls, as shown in Figure 3.1.

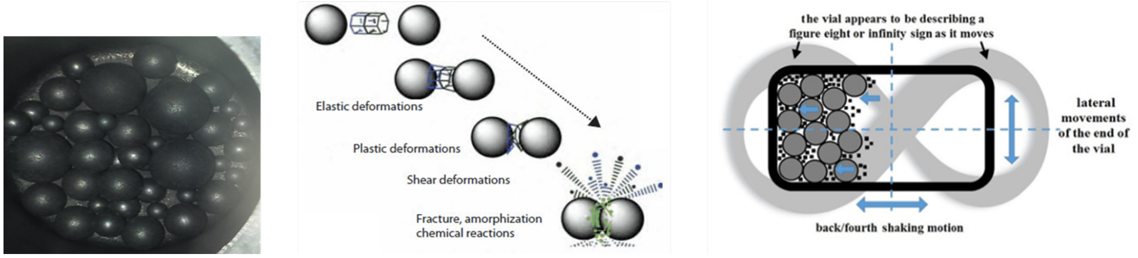

Figure 3.1. High Energy Ball Milling. Source: [22].

HEBM can both provide a way to enable chemical reactions, at lower temperatures, enabling the formation of cold alloys by forcing elemental inclusions both within and externally the initial crystal unit cell and reducing the grain size of the lattice [23]. The HEBM kinetic energy provided can enable the chemical inclusion of different elements into B_4C

lattice interstitial locations. The elemental inclusion enables placement in both lattice site locations and interstitial locations. Furthermore, the bonding strengths of B_4C support the preservation of the original lattice structure [8].

In addition to the ability of the HEBM to support elemental inclusions within the unit cell, the HEBM can support grain size reduction. Generally, the smaller the material grains, the harder the material becomes (Hall-Petch effect). The reduction of the grain size supports material strength, possible reduction of propagation of the amorphous shear band formation, and helps the elemental inclusion of Si within the B_4C unit cell.

The HEBM keeps the mixture temperature low ($\sim 200^oC$), while the local temperature reaches the level of 1500^oC because of the collisions [24]. The collision energy levels allow the Si to be inserted into the B_4C unit cell either by substituting local atoms or placed into interstitial locations. The integrity of the initial B_4C lattice is preserved, while defects created by the HEBM process support the elemental inclusion of Si within B_4C [8].

B_4C powder incorporated within this study used 700 nm (average grain size) from Electro Abrasives, Buffalo, NY. HEBM B_4C powders are analyzed to determine any changes in grain size and whether material strengthening occurs. In addition, HEBM of Si within B_4C powders are also studied. The stoichiometry of B_4C: Si is defined based on the atomic inclusion of one Si within every one atom of B_4C, where the ratio for one atom inclusion is presented below,

$$3\mathrm{B}_4\mathrm{C} + Si = B_{12} + 3C + Si \tag{3.1}$$

with atomic masses of B: 10.811 gr, C: 12.01 gr, and Si: 28.08 gr. So the ratio of one atom of Si is 28.08/165.7=0.169 based on the total weight of one $B_{12}C_3$ atom.

In order to produce the HEBM powders, a "dual chamber SPEX 8000" ball milling machine was used. The machine is able to run at 60 Hz with two containers working simultaneously. Each container has a volume of 65 ml containing a selected ball grinding media made using chromium steel [25]. The ball size distribution is presented in table 3.1. A powder mass to grinding media mass ratio from 1:8 to 1:10 was found to be more efficient in the powder milling process [8].

Table 3.1. HEBM Grinding Media

Chromium Steel Balls	3/8"	1/4"	1/8"
#	4	14	24

Each container containing between 5-6 grams of B_4C was subjected to a three-run cycle of 30 min with a 5min break between them, to let mixtures cool down and prevent clumping to the powder. In order to prevent clumping, a small amount of acetone (6-10 drops) per batch was added within the initial powder. Without the addition of acetone, excessive clumping was formed. The weight of each batch, in grams per container, is shown in the table 3.2.

Table 3.2. B_4C Alloy Stoichiometries

Stoichiometry of Mixing Powders			
Alloy Type	B_4C (gr)	Si (gr)	Zr (gr)
B_4C Ball Milled	3	0	0
B_4C:Si, 1/2 atom	3	0.508	0
B_4C:Si, 1 atom	3	1.016	0
B_4C:Zr, 1 atom	3	0	1.451

Calculations were performed to verify if HEBM provided enough energy to overcome the unit cell strength needed to insert elemental inclusions within B_4C [26]. To calculate a first-order approximation of the energies associated with the HEBM, Hugoniot 1D jump equations were used to measure the work and pressures induced on the B_4C unit cell to determine whether enough energy was imparted to enable elemental inclusions.

The Hugoniot Equation of State (EoS) $U_s - u_p$ relations were used to determine the work performed on the powder from different types of collisions between the powders and both the grinding media and container walls. Using the calculated particle velocities, the pressure and, consequently, the work done can be calculated and compared to the energy needed to enable the alloying of the B_4C powders. Based on the EoS, the relation between the shock and particle velocity is given by equation 3.2.

$$U_s = a + (bu_p) \tag{3.2}$$

where U_s is the shock velocity, a is the sound speed on the material of interest in (m/s), b is the particle velocity multiplier and u_p is the particle velocity. For B_4C the EoS is [22]:

$$\mathrm{B_4C}\text{: } U_s = 5170 + (2.78u_p) \tag{3.3}$$

while the chromium steel balls EoS is [27]:

$$\text{Chromium Steel: } U_s = 4722 + (1.441u_p) \tag{3.4}$$

The pressure at the impact point of the powder with the balls is given by the momentum equation:

$$P = \rho U_s u_p \tag{3.5}$$

where ρ is the density of the material being hit. The right and left-hand Hugoniot curves are given by the equations:

$$P = \rho(a + (bu_p))u_p \tag{3.6}$$

and

$$P = \rho(a + (b(u_r - u_p)))(u_r - u_p) \tag{3.7}$$

respectively. The densities in the right and left Hugoniot equations are not the same, and by impedance matching, the pressure during the impact is calculated. From the pressure and the impact area, the force can be calculated. Based on the unit cell strength, the work on the powder can be determined. The radius R of the impact point between spheres of R_1 and R_2spheres can be calculated using:

$$1/R = 1/R_1 + 1/R_2 \tag{3.8}$$

So the force according to the achieved pressure is calculated according to:

$$F = PA = P(\pi R^2) \tag{3.9}$$

The calculation of force per unit cell needs to calculate the number of cells in the area of impact between the spheres. Considering that the grain size of the "as bought" B_4C is 700 nm, the number of the particles is equal to:

$$N = A/A_{\mathrm{B_4C}} = A/(\pi R^2_{\mathrm{B_4C}}) \tag{3.10}$$

and the force per particle is:

$$F_{part} = F/N \tag{3.11}$$

From the force, the work produced is:

$$W_{part} = F_{part}(2R_{\mathrm{B_4C}}) \tag{3.12}$$

Dividing the work by the particle area, yields the work per area and is equal to:

$$W_{part} = P_{part}(2R_{\mathrm{B_4C}}) \tag{3.13}$$

with units (J/m^2) In table 3.3 are shown the energies related to the material-to-material or material-to-grinding balls impact.

Table 3.3. Spex HEBM Energies with Chromium Steel Balls. Source: [22].

Spex, u_p = 5.5m/s			
	Units	B_4C:B_4C	B_4C:balls
Pressure	Mpa	40	50
Force	μN	0.162	0.8143
Work	J/m^2	5.7	7.2

The numbers are shown that the energy provided by the impacts overcomes the fracture energy of 3.27 J/m^2 and the work to break the bonds [26].

3.1.2 X-Ray Diffraction (XRD)

The XRD enables the determination of lattice dimensions within a material. XRD enables measurements of the unit crystal size as well as chemical content for crystalline materials. XRD utilizes an X-Ray source of monochromatic photons, incident on crystalline material at specific (2-theta) angles. X-rays, with a specific wavelength, incident on a crystalline material with lattice spacings similar to the wavelength of the atomic spacing, diffract from periodic lattice spacings with both constructive and destructive interferences as the incident angle is varied (Figure 3.2). The diffraction pattern is collected through an X-ray detector. XRD enables the determination of lattice parameters, crystallite size, chemistry, and grain size. Every material has a unique X-Ray diffraction pattern, like the one shown in Figure 3.3. Moreover, any shift in the 2-theta angle can reveal some different alloys of the initial material (initial 2-theta angle) through changes in the unit cell dimension.

The XRD measurements performed in this thesis utilized a Rigaku MiniFlex 600 X-ray Diffractometer. The data was processed with Rigaku's PDXL software incorporating the ICDD PDF-4+ 2019 database. The samples were examined in powder form. A powder XRD is easier because powder provides all possible orientations. The diffraction pattern collected was analyzed using the Rietveld process [28]. Rietveld analysis provides an optimization of collected XRD peaks to interpret unit cell dimensions and crystallite size. The Rietveld method uses a predefined model for the structure observed. Every group of overlapping peaks diffracted by crystals oriented differently is examined based on the total integrated intensity, which is fitted to the predefined pattern. This way can reveal any shifts to the 1θ angle and lead to more robust results regarding the crystallite size and its volume [28].

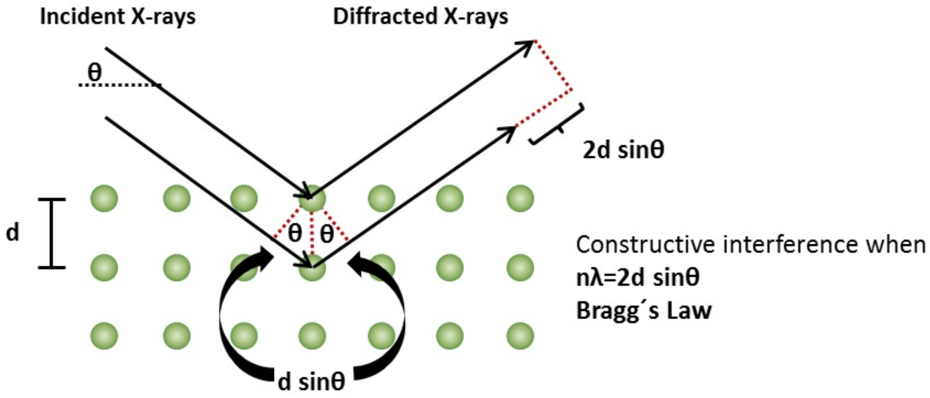

Figure 3.2. XRD Beam

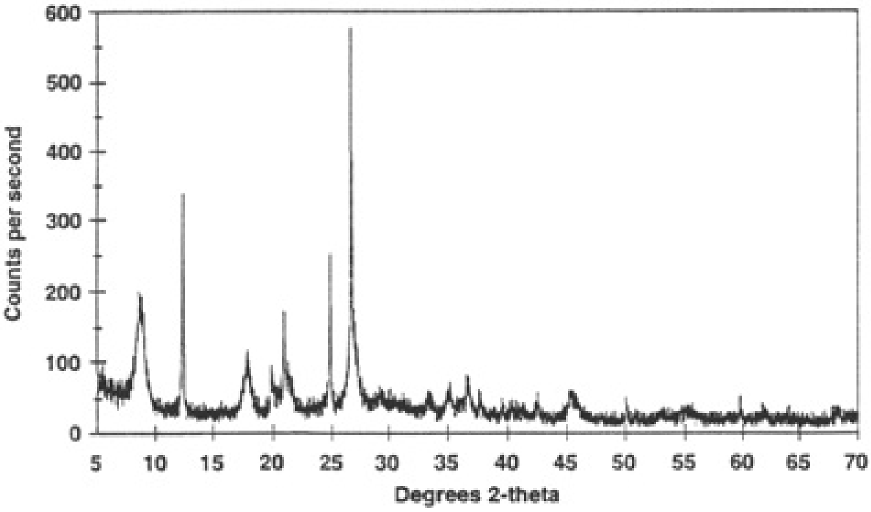

Figure 3.3. XRD - Unique Material Identity

Previous studies [8], [22] showed that the HEBM process leads to the expansion of unit cell volume and the reduction of the crystallite size of B_4C. Results of the study [8] are shown in Table 3.4 and Graph 3.4.

Table 3.4. B_4C XRD Data. Source: [8].

Sample	a(A)	b(A)	c(A)	$V(A^3)$	$\%\Delta V$	Crystallite Size (A)
B_4C	5.59737	5.59737	12.07149	378.2	-	314
B_4C,HEBM:Si, 1/2at	5.60561	5.60561	12.08961	379.89	0.445	242

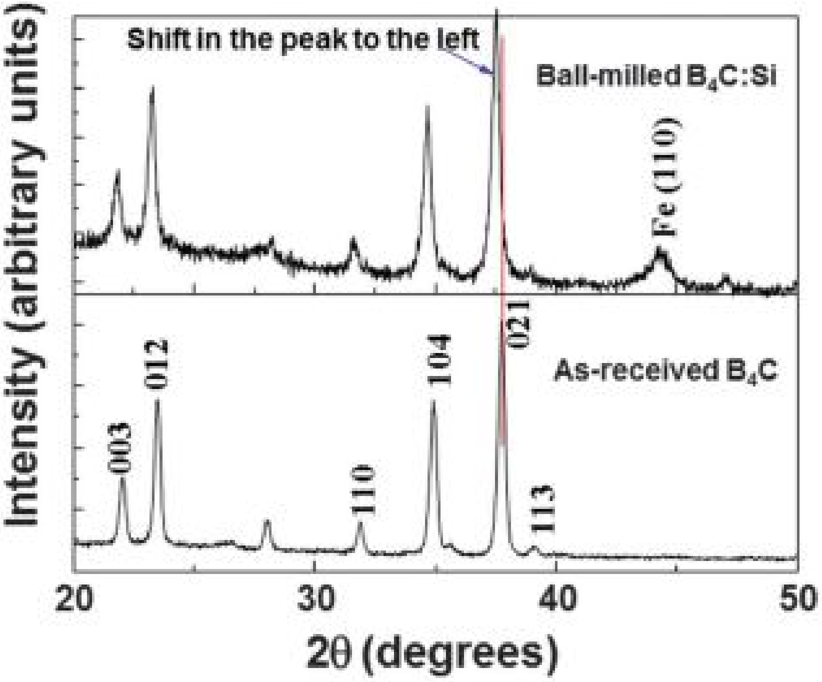

Figure 3.4. XRD 2θ Angle Shift to Left. Source: [8].

Even though the original crystal structure is not affected significantly as the 2θ pattern remains approximately the same, the shift to the left of the 2θ angle indicates an increase in the volume of the crystal lattice of the HEBM B_4C with Si inclusions. This study also examines the effect of the HEBM process on the B_4C lattice volume, showing that the HEBM process itself does not alter the lattice size. Furthermore, the volume expansion indicates that the Si substitution occurs only in 18% of the B_4C unit cells, even if the Si is enough to substitute all the unit cells.

3.1.3 Scanning Electron Microscopy (SEM)

The Scanning Electron Microscope SEM is a method to produce high-resolution images of a sample. A focused beam of high-energy electrons, emitted from a heated tungsten filament cathode, are accelerated through a high-voltage bias and focused on a material surface of interest [29]. The incident electrons excite secondary electrons from atoms on the material surface. The secondary electrons have energies around 50 eV which support low-depth penetration and enable the ability to collect electrons representative of the imaged surface. Back-Scattered Electrons (BSE) have higher energies and can be used to probe the chemistry but will not be discussed or applied for analysis. SEM must be performed under a high vacuum of $\sim 10^{-5,-6}\, torr$ chamber, shown in Figure 3.5, to enable a long enough mean-free path for imaging [29]. Unless the vacuum is present, the high-energy beam attenuates in the air and is unable to reach the sample at high-kinetic energy. Limitations of an SEM are that the sample should be solid, and the maximum dimensions should be approximately 10 cm in length and 4 mm in height. So, samples that produce various vapors or change their phase cannot be examined in a SEM.

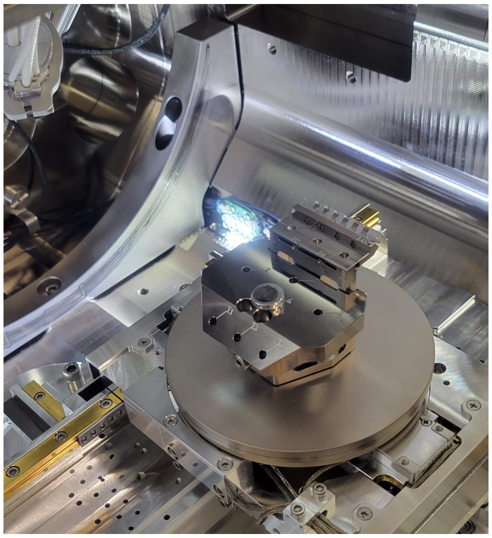

Figure 3.5. SEM Isolated Chamber

Powder samples of B_4C are collected directly after the HEBM process. They are attached to an electrically conductive tape (Figure 3.6). The conductive tape prevents charge build-up on the sample so as to avoid any noise in the images due to the accumulated charge in the sample from the incident beam.

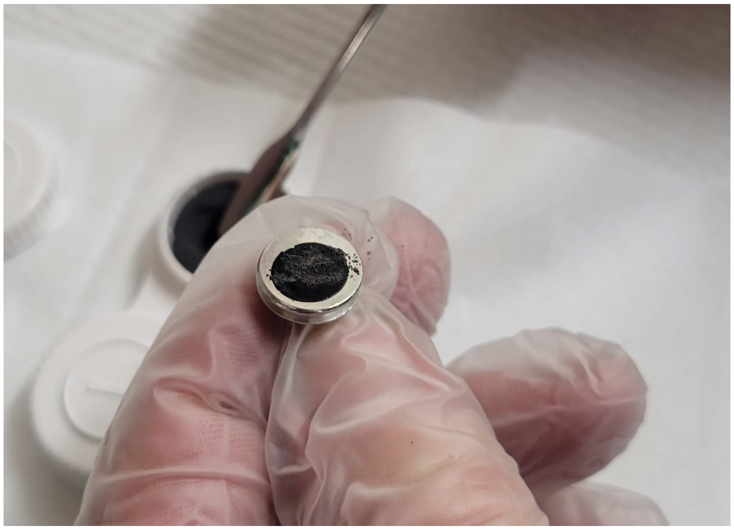

Figure 3.6. SEM Conductive Sample Fixture

SEM is based on a focused electron beam. The spatial resolution depends on the electron spot size that is altered according to the wavelength and the electro-optical system that generates the beam. Another factor that affects the resolution is the volume that interacts with the beam. Because the atom size is not comparable to the beam or the sample volume, the resolution cannot reach the atomic level. The system used was a "Thermo Fisher Scientific Helios 5UX." The corresponding images may reach a magnification of $1e + 5$, resolving particle sizes in the range of a few μm.

3.1.4 Hot Pressing

Hot pressing is required to produce B_4C due to the limited transportability of the chemical structure, which requires both heat and pressure to densify the powder and reach densities close to Theoretical Maximum Density (TMD). As mentioned previously, the formation of B_4C requires a pressure of 3000 psi and a temperature of 2200^o C. Thus high external pressure is applied to support the compaction of the B_4C powder. All of the powders were hot-pressed by SCI Engineering in Columbus, Ohio. A graphic representation of the Hot Pressing process is shown in Figure 3.7.

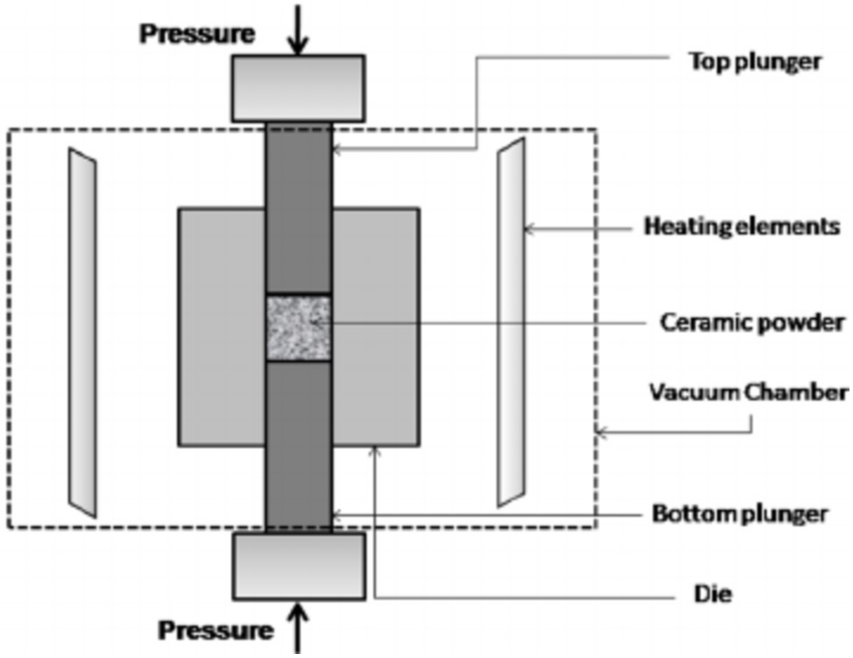

Figure 3.7. Hot Pressing

The TMD of B_4C is approximately $2.52\,gr/cm^3$ [22]. The TMD of B_4C with elemental inclusions increases at the value of $2.773\,gr/cm^3$ for B_4C: 1 atom Si and $3.733\,gr/cm^3$ for the B_4C: 1 atom Zr.

3.1.5 Hardness Test

High hardness is the fundamental reason for using ceramics in front face armor plates. By conducting a hardness test to B_4C disks, it is ensured that B_4C hardness is kept despite the elemental inclusion or even better if it is changed by this. The Vickers test was used to check each sample's hardness. For B_4C as bought powder, the expected hardness is 30 GPa in the Vickers scale [9]. Vickers test uses a diamond shape indenter with a square base and an angle of 136^o. which touches the target surface with a specific force of 9.8 Nt for 15 seconds. This leaves a squared diamond shape footprint on the material face whose diagonals are measured as shown in Figure 3.8. The equation which describes Vickers' test calculates the

Vickers' value using these two diagonals and the applied force [30]. The hardness tests were conducted using a "phaseII 900-390" device.

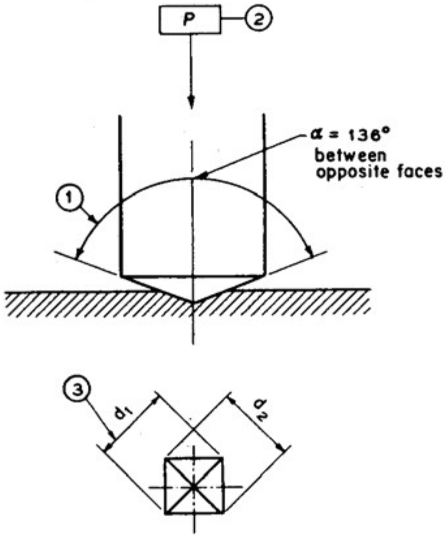

Figure 3.8. Vickers Hardness Test

It should be noted that porosity or surface inhomogeneity can alter the calculated values. This is very obvious in Figure 3.9, where the surface grains are shown very clearly.

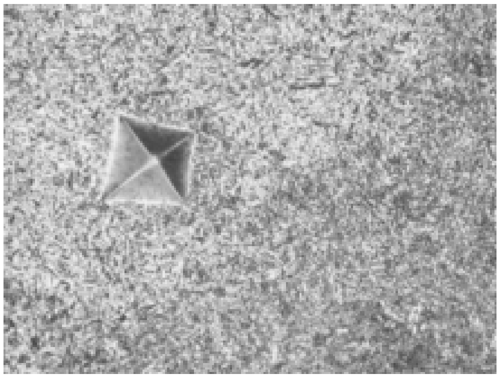

Figure 3.9. Material Surface Grains and Vickers' Footprint

The surface roughness makes it harder to evaluate the limits of the diamond footprint. For unpolished surfaces, the hardness measurements may vary from point to point, even if the measurement locations are very close to each other. Thus the ceramic target disks should be polished to achieve better hardness results with fewer variations and to ensure that their surfaces are planar and parallel to each other.

The device used for the polishing is from Allied High Tech Products Inc., shown in figures 3.10. It has a rotating head and a rotating table, and their rotational speeds can be adjusted independently. The head is pressed against the table with air pressure either through the center axle of rotation (figure 3.10a) or through individual pistons (figure 3.10b) with force adjusted by the user.

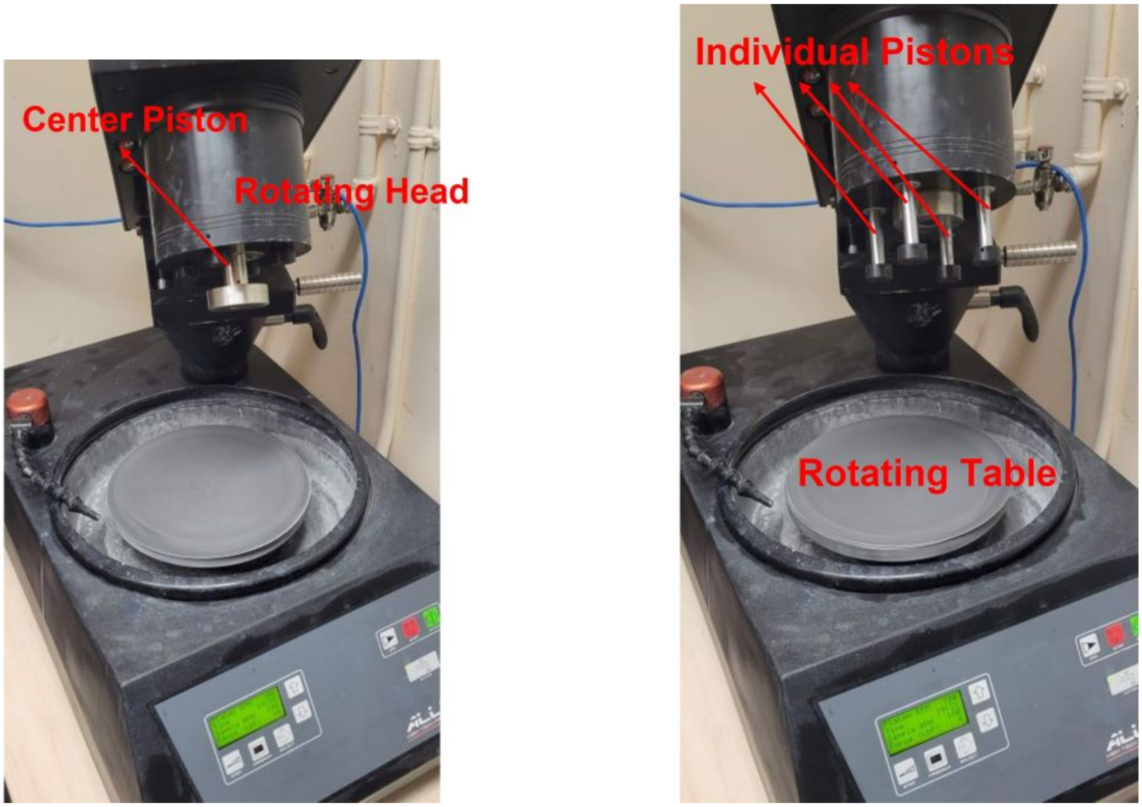

(a) (b)

Figure 3.10. (a) Polishing Device - Center Piston Force (b) Polishing Device - Individual Piston Force

The ceramic disks were placed on six individual bases, which in turn were tightened onto the main fixture of the rotating head. This was because each sample had a different thickness, so individual adjustments were needed to ensure that each sample touches the table evenly. To distribute the force evenly across the rotating fixture, a flat disk was placed between the fixture and the head to transfer the pressure to the fixture uniformly.

The targets were polished in 2 cycles of 15 min each using 9, 6, and 3 μm diamond solution. The applied force was from 10 to 20 lbs using the individual piston option. The head was set to rotate counterclockwise to the table so that the polishing solution always remains in contact with the targets on the inside area, avoiding extra loss of polishing medium. The rotating speeds were set at 300 rpm for the head and 50 rpm for the table because, at greater rotational speeds, the polishing solution was pushed away by the centrifugal force and could not stay in contact with the targets. A polished target vs. a not-polished one is shown in figure 3.11.

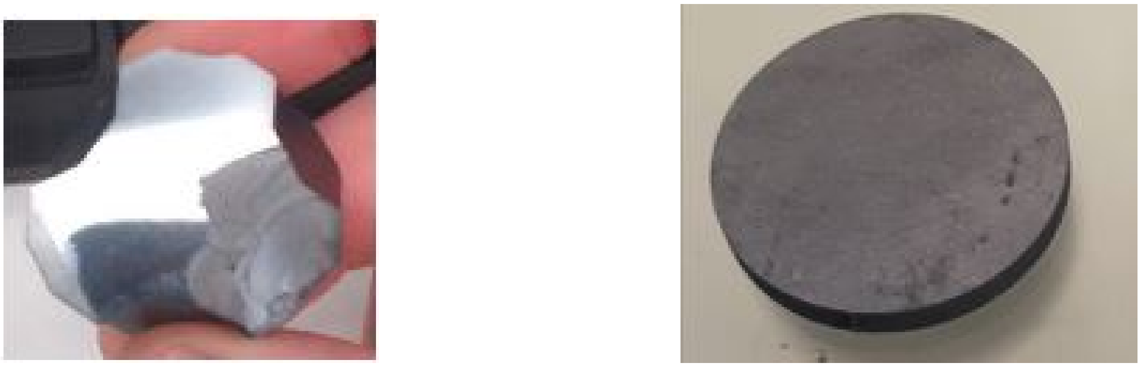

(a)

(b)

Figure 3.11. (a) Polished Target Surface. Source: [22]. (b) Unpolished Target Surface.

3.2 Gun System

A 40 mm single-stage smooth bore powder gun was used to accelerate impacting flyer plates to enable impactor velocities up to 2.7 km/s. The gun system is manufactured by Physics Applications Inc (PAI). The launch tube has a length of 5.5 m. Just beyond the gun muzzle, instrumentation includes a laser velocimeter Photon Doppler Velocimetry (PDV) and four shorting pins (located 90^o apart) assembly to enable the equation of state/impact studies to be performed. Beyond the instrumentation, a catch tank enables the arrest of the projectile through a series of 24 $1/4$" steel plates. Figure 3.12 represents the gun fixture allocation. The entire gun system is pulled to a vacuum of $\sim 100\,mtorr$. The vacuum reduces both the blast pressure within the tank and reduces gas trapped between the projectile and target, which, under rapid compression, can elevate the impact temperature.

Figure 3.12. 40 mm Powder Gun System

The propellant charge uses a sting tube to place the main propellant. Within the center of the sting tube Benite strands are placed to enable a uniform burn of the main propellant charge. Two different sting tubes are available for the gun system. For lower velocity shots, a short sting enables charges up to 300 grams, and a long sting enables charges up to 700 grams, as shown in Figure 3.13. The main charge used is HODGDON H50BMG 50 caliber propellant. The firing sequence is initiated by a 300 Winchester Magnum cartridge with 1.5 grams of Hodgdon 777 (Figure 3.15). The center of the sting tube uses enables 11 Benite sticks, which burn faster than the powder enabling the uniform burn. The Benite sticks are shown in Figure 3.14. Their location in the middle of the hollow tube and their faster burning produce a uniform radial flame propagation which improves the powder initiation and even burning while it prevents any traveling waves from forming. The final charge assembly is shown in Figure 3.16.

Figure 3.13. Propellant Loading Tube

Figure 3.14. Benite Sticks

Figure 3.15. Prime Propellant

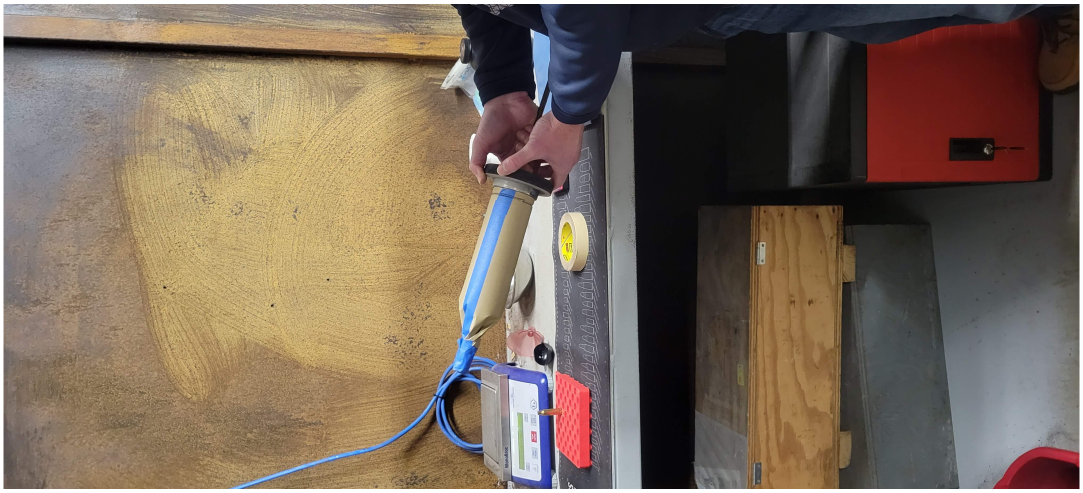

Figure 3.16. Final Propellant Assembly

The propellant is loaded into the gun breech and it is secured by a breech plug using acme threads to fasten to the breech, (Figure 3.17). To initiate the 300 WinMag cartridge, a solenoid with a plunger is used to drive the firing pin. The solenoid utilizes a 200 V capacitor that discharges into a solenoid driving the plunger into the firing pin enabling the initiation of the WinMag percussion primer and the firing chain. All the components that participate in the firing procedure are depicted in Figure 3.18.

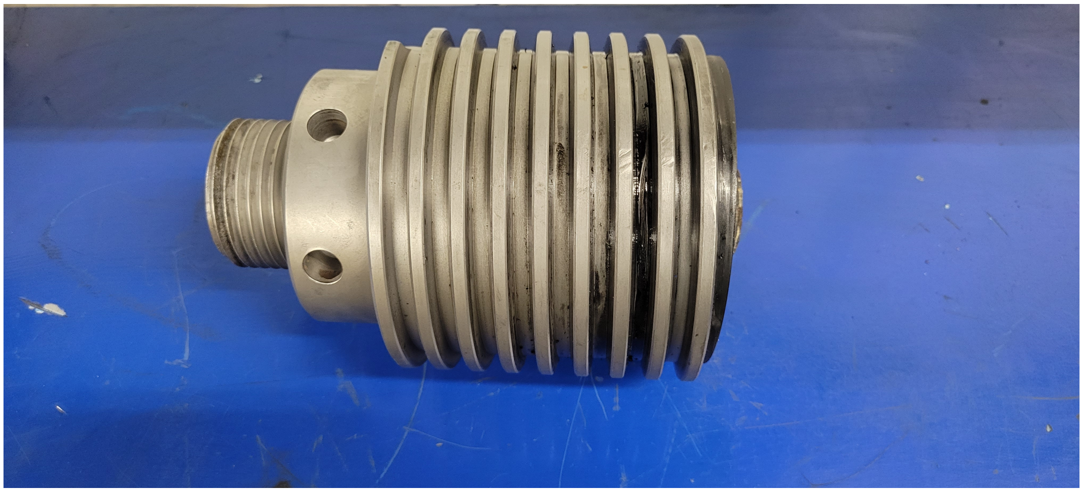

Figure 3.17. Breach Securing Plug

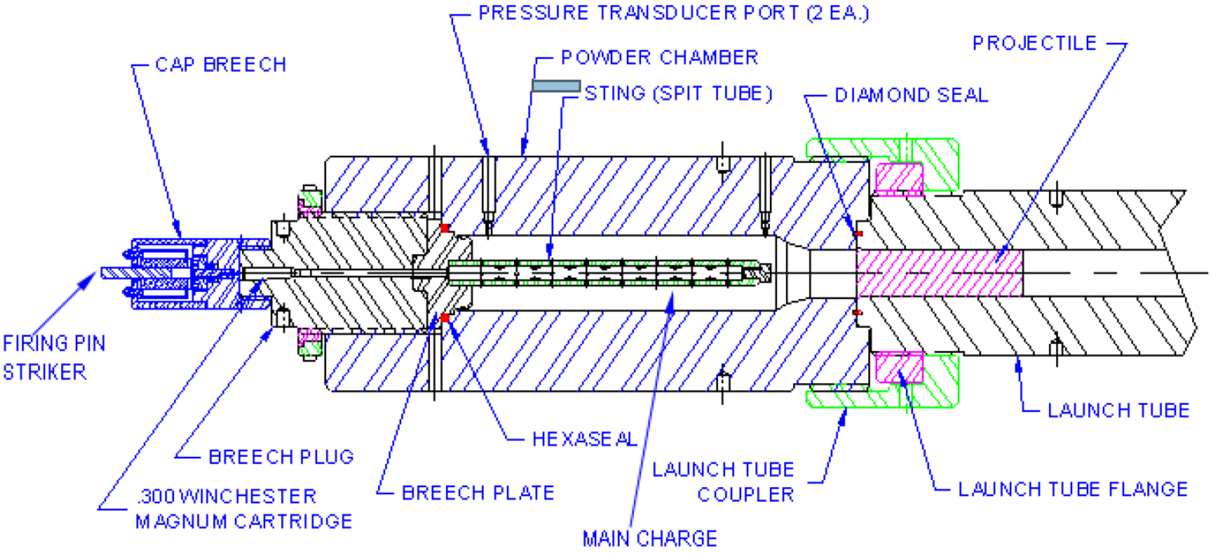

Figure 3.18. Breach Graph

3.3 Target and Projectile Assemblies

3.3.1 Target

The impact on the projectile-target surface must be planar in an 1D shock impact experiment. To enable high planarity, the shot line axis should be aligned perpendicular to the impact plane. The target fixture shown in Figure 3.19 is precisely aligned using spring-loaded washers, enabling perpendicular alignment to the shot line. A proximity sensor loaded into the gun barrel and rotated enables planarity adjustment to 0.001” deviation within a 1” radius circle, Figure 3.20.

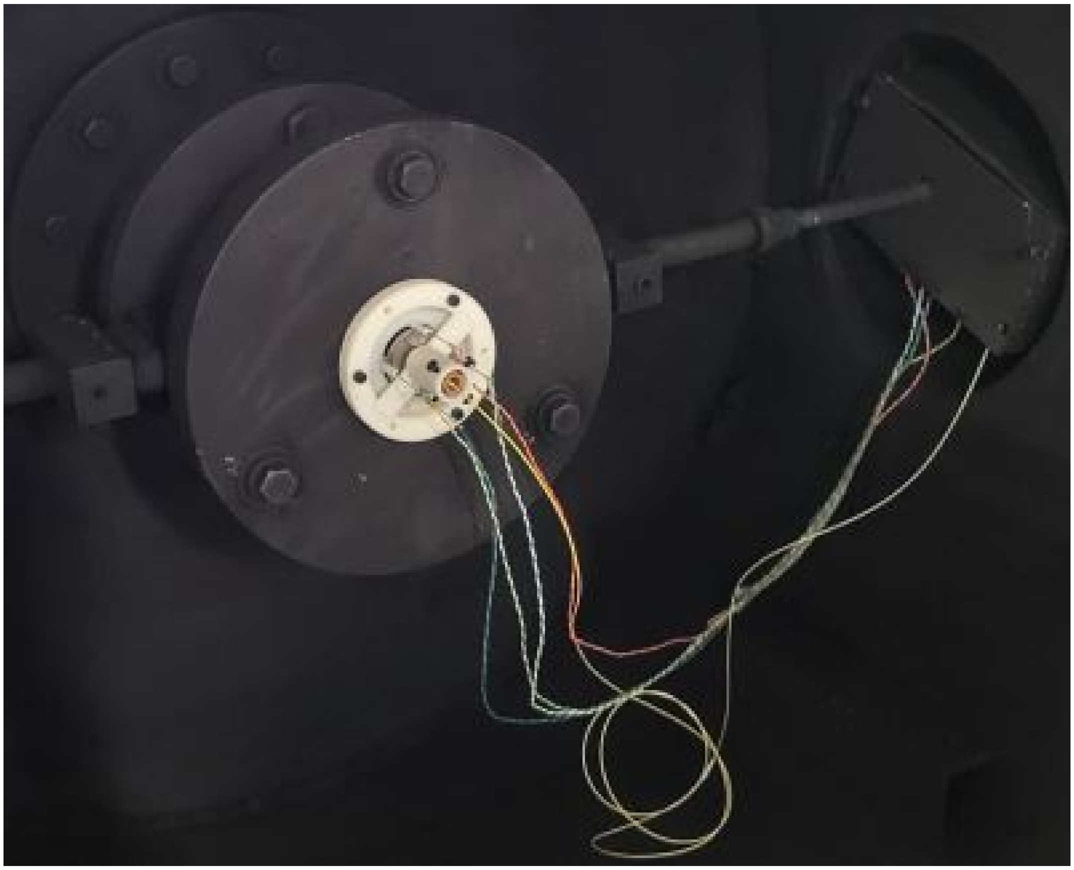

Figure 3.19. Gun Side Target Fixture

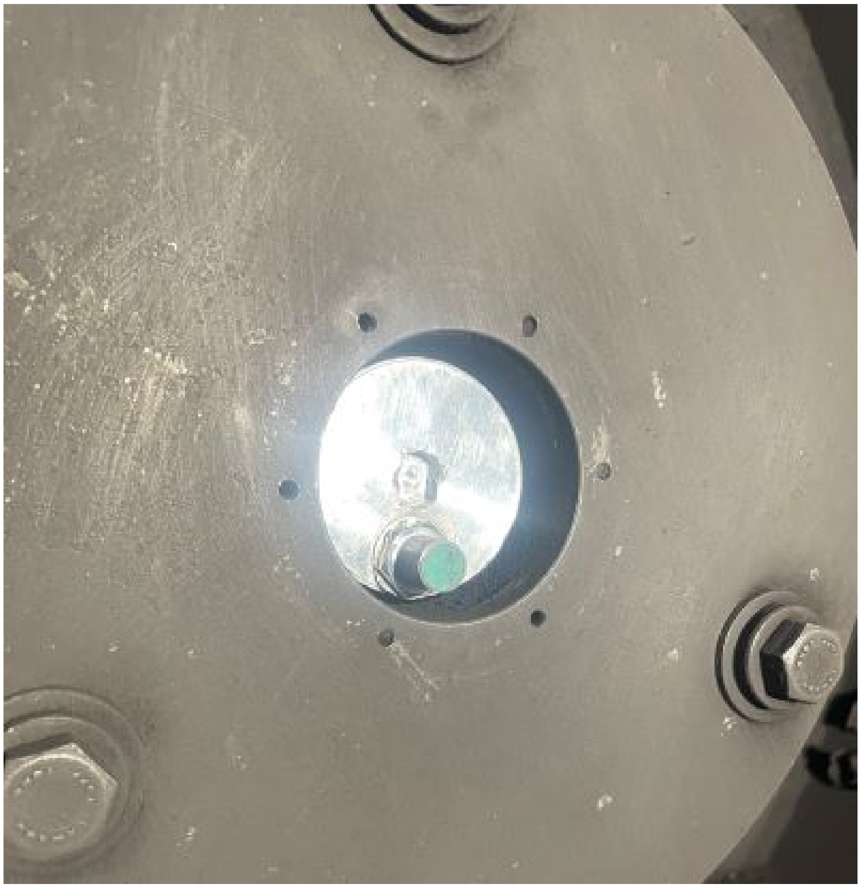

Figure 3.20. Proximity Sensor Check

The 3D printed target base, shown in Figure 3.22, mounts to the gun system target plate. The target assembly was performed through construction on a flat glass base to enable a uniform flat reference for both the target impact face and shorting pins. The whole assembly was adhered together once all components are properly aligned along the base window plane using a Hardmann two-part epoxy. The cylindrical fixture on top of the holder mounts the PDV probe. The PDV holder allows alignment of the PDV with the target using the four black screws.

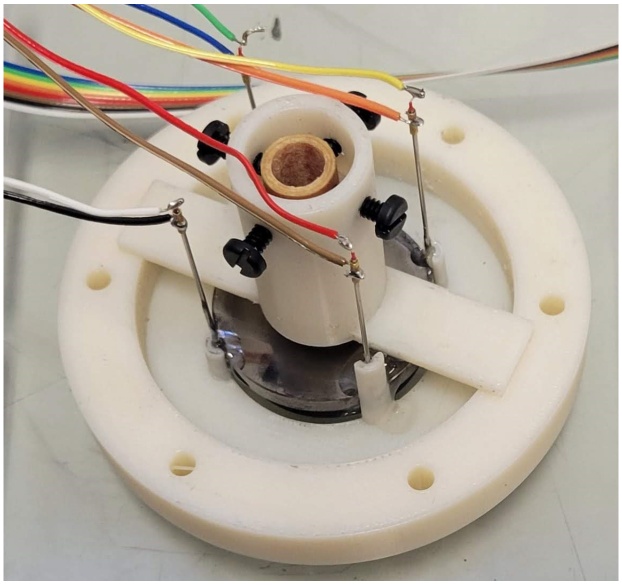

Figure 3.21. Target Assembly

Figure 3.22. Target Holder

3.3.2 Shorting pins

A shorting pin is a switch that enables conduction when impacted. It consists of a hollow conductor tube with an inner conductor core, isolated from each other. When this assembly is hit by a conductive surface, a short occurs. When the shorting pins are impacted, a small capacitive circuit is discharged, enabling a voltage spike to be generated and sent to a recorder (oscilloscope). The typical outline of a shorting pin is shown in Figure 3.23, and the generated pulse of four simultaneous pins is shown in Figure 3.24.

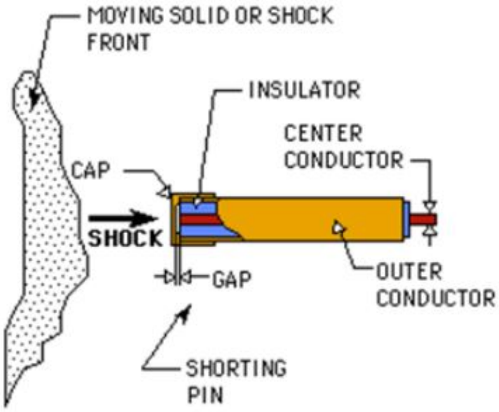

Figure 3.23. Shorting Pin

The capacitive discharge circuit enabling the voltage pulse is housed within a Dynasen pin mixer model CS2-50-300 providing a $\sim 30\,V$ discharge signal when the pin shorted.

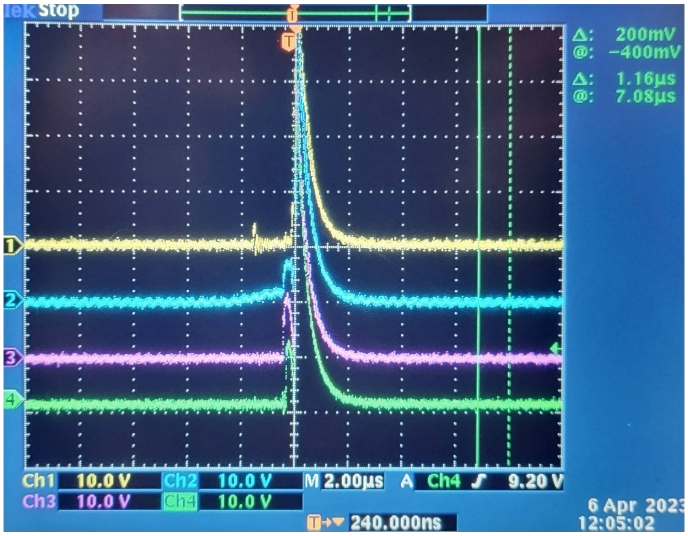

Figure 3.24. Impact of 4 Shorting Pins Generating 4 Pulses

These voltage pulses can be utilized to both trigger the PDV measurements and extract the orientation of the impactor at the moment that it hits the target. The planarity can be calculated based on the angle between the projectile velocity and the normal vector to the impact surface. The projectile velocity vector is actually the cross-product of the vectors that are formed by the four timestamps (taking each pair of anti-symmetric pins), given that the impactor is moving to a constant speed measured by the laser photo-detectors, described in section 3.4.2. A graphical representation of the impact planarity assessment is shown in Figure 3.25.

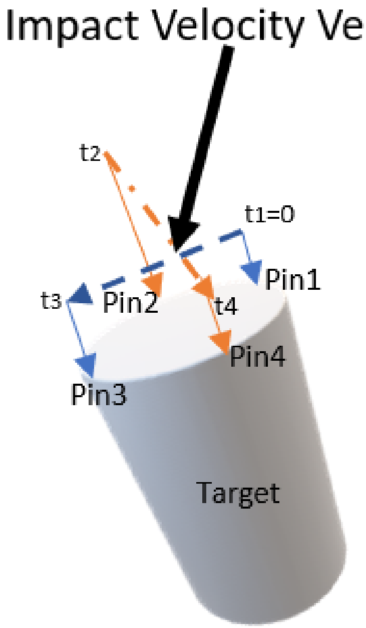

Figure 3.25. Impact Planarity Representation

By using the time that pin1 is hit as the origin of time t_1, the rest of the real timestamps can be calculated from the differences of when the voltage spikes occur. By knowing the impactor velocity magnitude from the laser photo-detectors(section 3.4.2), the distance dx traveled by the impactor between the two pin impact timestamps can be calculated from the equations 3.14.

$$\begin{aligned} dz_{31} &= V_{impactor} * (t_3 - t_1) \\ dz_{42} &= V_{impactor} * (t_4 - t_2) \end{aligned} \tag{3.14}$$

Using the pre-measured diameter of the target, the angles of the colored dashed vectors and the impact surface, (shown in Figure 3.25), can be calculated from the equations 3.15.

$$\begin{aligned} \theta_{31} &= tan^{-1}\left(\frac{dz_{31}}{D_{target}}\right) \\ \theta_{42} &= tan^{-1}\left(\frac{dz_{42}}{D_{target}}\right) \end{aligned} \tag{3.15}$$

With this information, the two dashed vectors in Figure 3.25 can be represented according to the equations 3.16.

$$\begin{aligned} Vector_{31} &= (D_{target})\hat{x} + (-dz_{31})\hat{z} \\ Vector_{42} &= (D_{target})\hat{y} + (-dz_{42})\hat{z} \end{aligned} \tag{3.16}$$

The cross-product is calculated according to equation 3.17,

$$\overrightarrow{V_{imp}} = \begin{vmatrix} \hat{x} & \hat{y} & \hat{z} \\ D_{target} & 0 & -dz_{31} \\ 0 & D_{target} & -dz_{42} \end{vmatrix} \tag{3.17}$$

and the result is shown in equation 3.18.

$$\begin{aligned} V_{imp} &= V_{imp}^{x}\hat{x} + V_{imp}^{y}\hat{y} + V_{imp}^{z}\hat{z} \\ V_{imp}^{x} &= +D_{target}dz_{31} \\ V_{imp}^{y} &= -D_{target}dz_{42} \\ V_{imp}^{z} &= +D_{target}^{2} \end{aligned} \tag{3.18}$$

Finally, the angle θ_{imp} between the normal to the impact surface and the cross-product V_{imp}

is calculated from the equation 3.19.

$$\cos\left(\theta_{imp}\right) = \frac{\overrightarrow{V_{imp}}\vec{z}}{|V_{imp}||\vec{z}|} \tag{3.19}$$

3.3.3 Projectile

The projectile is constructed using a solid polycarbonate cylinder. Within the projectile, two grooves are machined to enable two o-rings to seat and seal the interface between the projectile and gun barrel enabling a vacuum to be pulled prior to firing. The projectile diameter is $\sim 40\,mm$ with an overall length of $85\,mm$. The projectile is shown in Figure 3.26.

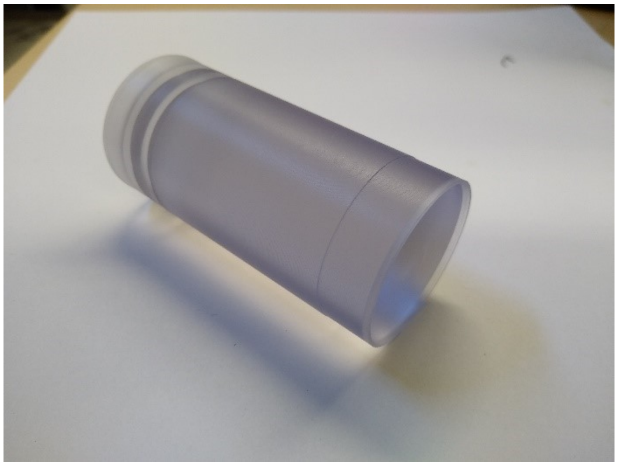

Figure 3.26. Projectile Sabot

The front face of the projectile enables the mounting of the front flyer plate and aluminum ring mount. The aluminum ring supports both the mounting of the flyer plate and enables triggering of the shorting pins during impact, subsection 3.3.2. The impactor used for this thesis includes both an Oxygen Free High-Conductivity (OFHC) copper disk (diameter of 34 mm and a thickness of 6 mm) and B_4C or B_4C with elemental inclusion disks. This disk impactor is shown in Figure 3.27.


Figure 3.27. Copper Impactors

The assembly of the sabot, the impactor, and the aluminum disk has a mass of approximately 180 gr, shown in Figure 3.28.

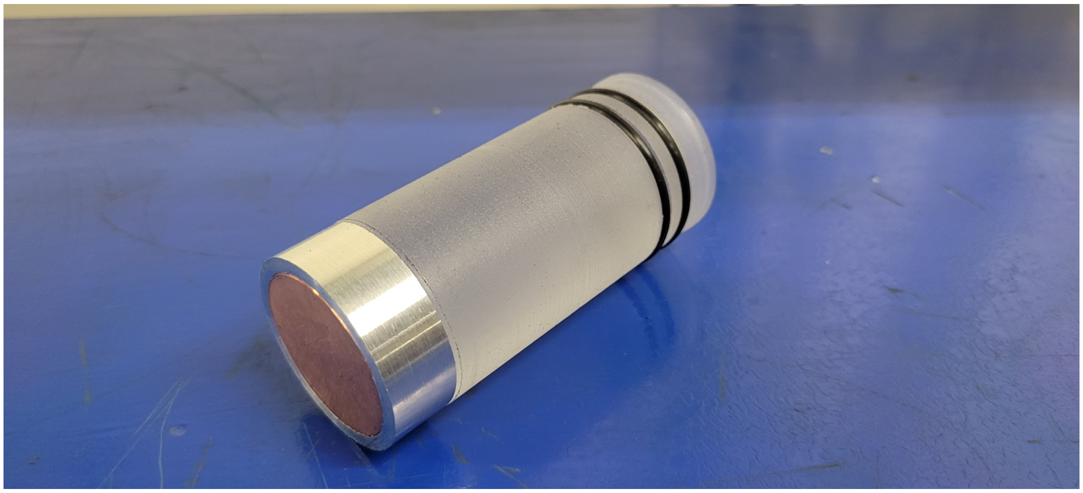
Figure 3.28. Projectile Assembly

3.4 Instrumentation

3.4.1 Photon Doppler Velocimetry (PDV)

The velocity measurement in shock physics experiments is the primary diagnostic. Explosive blasts or high-velocity impacts can drive impacted surfaces to high velocities (km/sec). PDV enables picosecond resolution of particle velocity measurements of the impactor/projectile interfaces. A Homodyne PDV component representation is shown in figure 3.29.

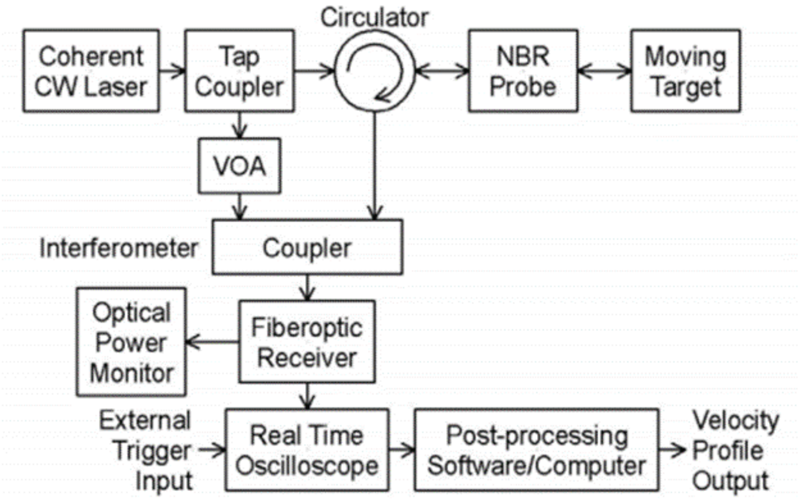

Figure 3.29. Homodyne PDV. Source: [22].

A Homodyne PDV system utilizes a single-mode laser that illuminates a surface via a single-mode compatible Non-Back-Reflecting (NBR) collimator. From the initial output beam, 99% is sent to the target surface, while the rest 1% is routed through a Variable Optical Attenuator (VOA) to the coupler that also receives the reflected signal from the surface. Using a voltage adjustment, the intensity of the 1% signal from VOA can be matched to the intensity of the reflected one from the target surface. Considering that the two amplitudes are properly adjusted, the two signals are mixed together in real-time into the coupler, while the surface is moving, producing a beat signal. The beat signal is the constructive interference of the target beam with the tapped-off reference signal. The frequency of this signal is related to the Doppler shift of the source beam frequency because of the surface velocity. A higher frequency (Doppler up-shift) is caused by relative signal compression (motion towards the sensor) while a lower one (Doppler down-shift) is caused by relative signal stretching (motion away from the sensor). The beat frequency is dependent on the surface velocity [22].

The velocity measurements within this study incorporated Heterodyne Velocimetry. This method uses two laser beams to produce the beat signal. In a Heterodyne system, the velocity is related to the measured frequency of the beat waveform captured by digitizers.

In a Heterodyne system, the light that illuminates the surface (red beam in figure 3.30) mixes with a reference laser beam that is already shifted in the wavelength (blue beam in figure 3.30). The shifted reference beam is mixed with the projected laser incident on the surface. The amount of light from both beams that reaches the detector is approximately the same. The constructive interference of these beams generates a waveform with a specific beat frequency, that is captured in the detector and stored by the digitizer, as shown in figure 3.30. This beat frequency simulates the generated waveform produced by mixing the original beam and the same shifted reference beam. Through the shifted reference laser, the PDV is able to detect a beat frequency even when the target is at rest.

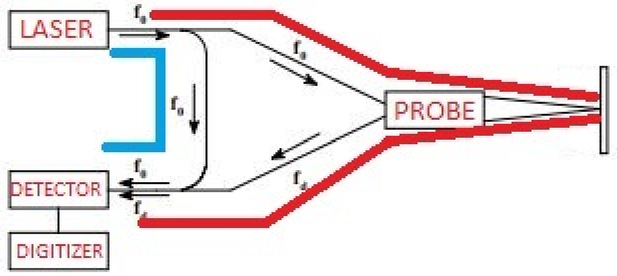

Figure 3.30. Heterodyne Velocimetry Method

In the case that the stationary surface starts moving as shown in figure 3.31, the already Doppler-shifted beam (red beam) departing from the laser, is reflected back with an even greater shift in the wavelength (purple beam). When the purple beam is mixed with the original beam (blue beam), produces a different beat frequency waveform than in the stationary surface case. This difference in the beat frequency waveform is transformed into the velocity of the free surface.

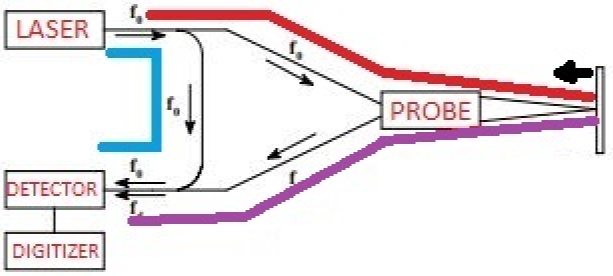

Figure 3.31. Heterodyne Velocimetry onto a Moving Surface

The intensities of the two beams, sent to the detector, are adjusted to be similar enabling the beat frequency. The time-dependent intensity captured by the detector is given by the equation 3.20, as shown below:

$$I(t) = I_o + I_d + \sqrt{I_o I_d} sin(f_b(t)t + \phi) \tag{3.20}$$

where I_o and I_d are the intensities of the original and the Doppler-shifted beam, respectively, f_b is the beat frequency, and ϕ is the relative phase between the two beams. The intensity related to the constructive interference of the two beams is calculated based on the first two terms of the equation 3.21 while the third one gives the beat frequency data. The beat frequency is computed using the:

$$f_b(t) = |f_d(t) - f_o| \tag{3.21}$$

and it is transformed into velocity using the:

$$f_b(t) = 2\frac{v(t)}{c} f_o \tag{3.22}$$

where c is the speed of light. A characteristic of a heterodyne system is that the f_b is computed based on the absolute value of the frequency difference. So, the movement towards or away from the probe cannot be detected.

For a heterodyne PDV working beyond the visible range, at 1550 nm wavelength, the f_o corresponds to several GHz. If the measured velocity is in the range of 1 - 3 km/s, the f_b lays in the range of 1 - 5 GHz. At this point, it should be explained why using the

Heterodyne method in combination with lasers beyond the visual range can be a better option for high-velocity impacts of some km/s. For example, if the laser emits at $\sim 500\,nm$ and the measured velocity is 1000 m/s, the f_b would be $3.7\,GHz$. However, if the laser emits at $1550\,nm$, the f_b would be $1.3\,GHz$ for the same measured velocity. So, by applying the Nyquist theorem, the digitizer should be capable of sampling at least twice the measured frequency. So, the visible range laser would need a digitizer bandwidth of $7.4\,GHz$ while the $1550\,nm$ laser would need one with $2.6\,GHz$.

The Heterodyne Velocimeter operates at the $1550\,nm$ (Figure 3.32a). The oscilloscope used to capture the data is a Tektronix TDS6154C with a bandwidth of $15\,GHz$ and a capability of $40\,Gsamples/sec$, shown in Figure 3.32b. The oscilloscope is equipped with a 64 MB memory module, which means that can store limited samples of data considering the storage demanded for each sample. So, the oscilloscope is set to $(1.5\,Gsamples/sec)/(Km/sec)$ of horizontal resolution to capture the time window within which the impact is taking place.

(a) (b)

Figure 3.32. (a) Heterodyne Velocimeter (b) PDV Oscilloscope

A typical image of good-quality data is shown in Figure 3.33, where the large amplitude is referred to the preimpact time while the surface is stationary and the smaller amplitude is during the surface movement after the impact. As it is obvious from examining the figure, the amplitudes of the pre-impact signal and post-impact signal are different. This change is caused by the alteration of the surface transparency after the shock wave passes through it and the changes in laser reflectivity while the surface moves.

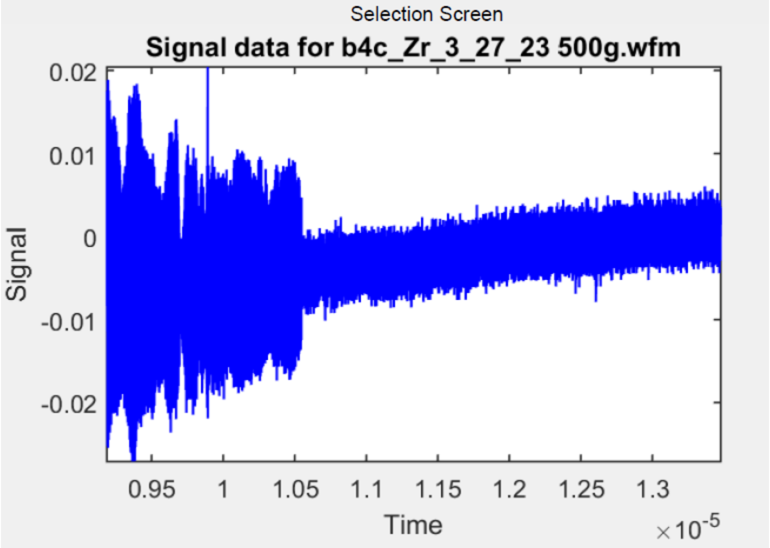

Figure 3.33. PDV Data Captured in Oscilloscope

The data captured are fed into the Sandia InfraRed HEterodyne aNalysis (SIRHEN) program, which applies a Fourier analysis producing a plot of the beat frequency over the total time of data recording, shown in Figure 3.34a. Further analysis by advancing the program's steps is to transform the frequency graph into a velocity graph, shown in Figure 3.34b. To do so, the program applies the equation 3.22, while the f_o is known and the f_b is already calculated. At this point, it should be noted the residual velocity existing in the graph before the impact, shown with a black horizontal line in Figure 3.34b. This velocity is calculated based on

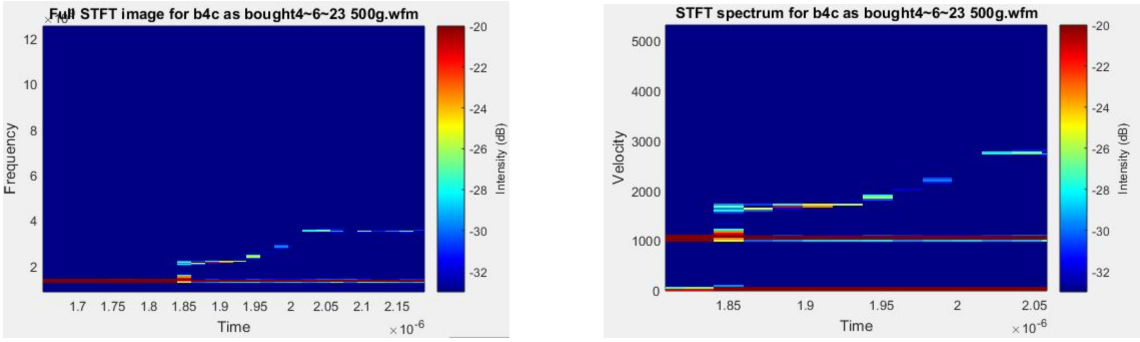

(a) (b)

Figure 3.34. (a) PDV Frequency Graph (b) PDV Velocity Graph

the beat frequency between the original and the shifted beam, before the impact. So, the velocities gathered by the graph of Figure 3.34b should be reduced by this amount to depict the actual surface velocity after the impact.

3.4.2 Pre-impact Laser Velocity Photodetectors

The incident velocity is measured using a three-laser photodetector system, shown in Figures 3.35 and 3.36. This system incorporates three lasers of 5 mW and three photodetectors with a wavelength of 632 nm. The lasers are separated by a distance of 1", and the collected light uses a fiber optic laser channeling the light to three separate photodetectors shown in figure 3.35. Each photodetector output signal is captured by an oscilloscope individually, as it is shown in Figure 3.37.

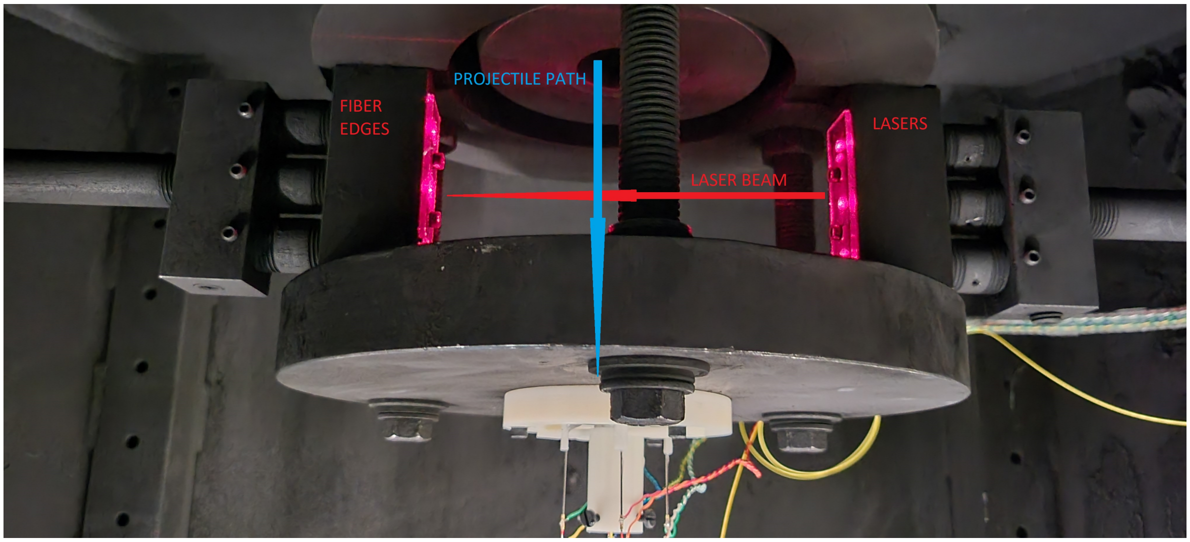

Figure 3.35. Photodetector's Lasers and Receiving Fibers

Figure 3.36. Photodetector's Main Module

Before the impact, each laser is aligned to each fiber and the signal produced by the photodetector has an output of $\sim 0.5\,V$. When the impactor passes through the laser path, it cuts the laser beam transmission which is detected by the photodetectors resulting in a vertical drop of voltage magnitude captured on the oscilloscope, as shown in figure 3.37. By tracking the timestamps difference (dt) of each drop and knowing the separation distance between the beams, the pre-impact velocity is easily calculated by the equation 3.23.

$$V_{imp} = 1\,inch/dt \tag{3.23}$$

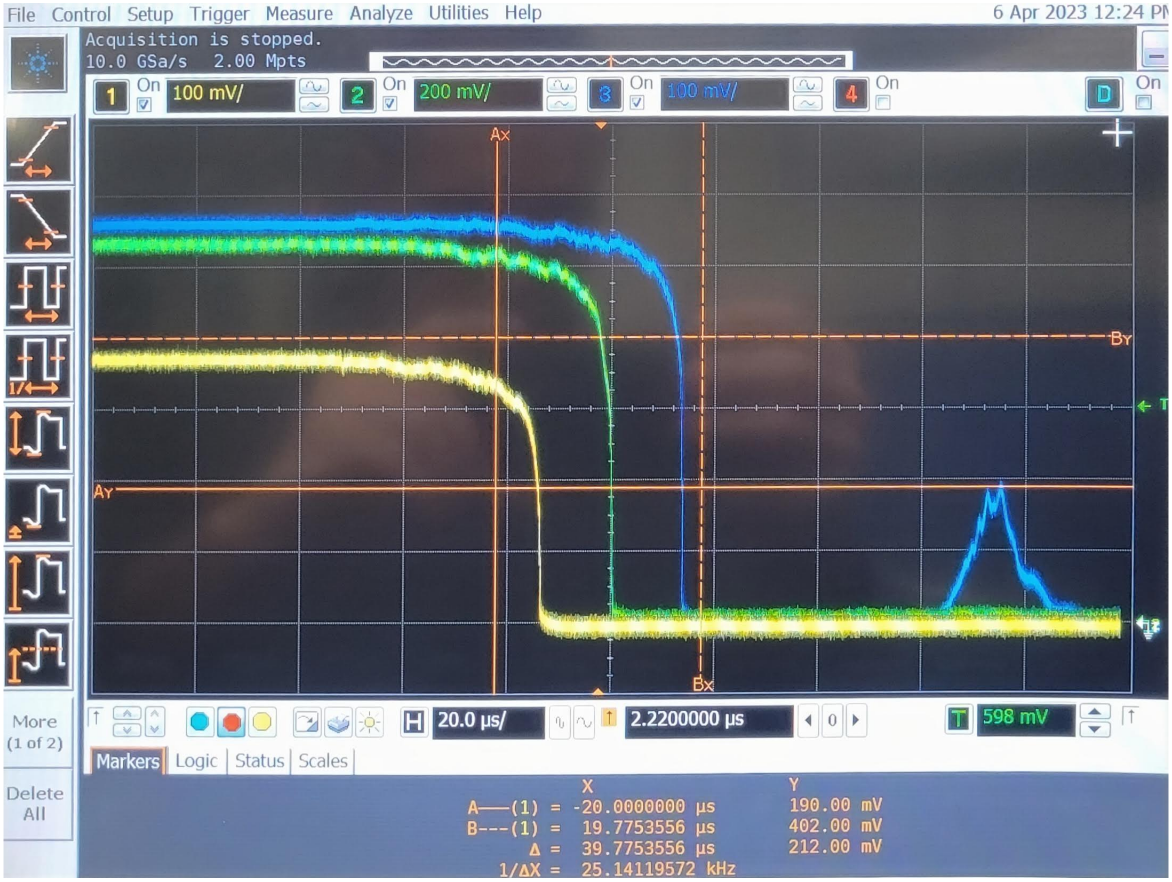

```
Acquisition is stopped.
10.0 GSa/s   2.00 Mpts
```

```
                    X                  Y
A——(1) = -20.0000000 µs        190.00 mV
B---(1) =  19.7753556 µs       402.00 mV
     Δ =   39.7753556 µs       212.00 mV
  1/ΔX =   25.14119572 kHz
```

Figure 3.37. Laser Photodetector Oscilloscope Output Graph

3.5 Shock Physics Theory

Shock physics investigates the material response under high-pressure/strain rate impacts. These impacts subject the material to high dynamic loading conditions where formed shock waves are generated and propagate through the material. These shock loading conditions can be initiated into a solid material either by high-velocity impacts, between a projectile and a target, or by an explosive. Regardless of how the shock wave into the target was generated, the material experiences an abrupt large compressive stress in a very short time period (ns) and is subjected to a condition called "Uniaxial Strain Loading." The design of the experiment enables the application of 1D Hugoniot jump conditions where three simple conservation equations (mass, momentum, and energy) enable the determination of impact pressures, density changes, and changes in internal energy of the impacting materials.

3.5.1 Uniaxial Strain Deformation

Uniaxial strain loading is the condition in which a material is deformed only in one dimension. Under this condition, the material is constrained and cannot expand in any of the lateral axes of loading (y,z), where longitudinal compression due to a fast-moving shock wave and geometric constraints enable uniaxial compression to remain until relief waves arrive (Figure 3.38) [31].

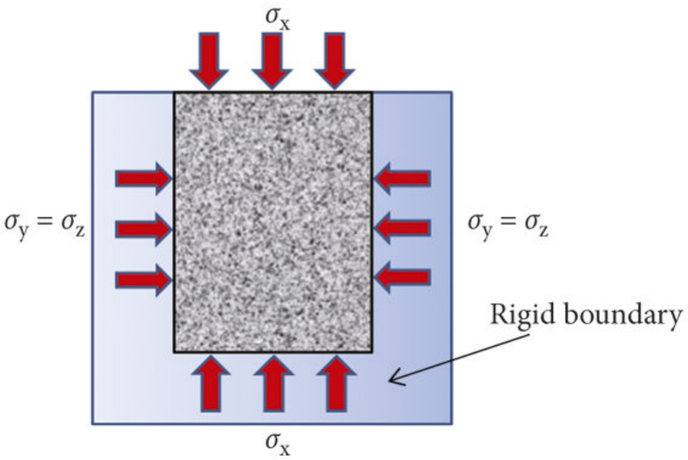

Figure 3.38. Uniaxial Strain in X Direction

In this situation, the strains in the lateral directions are zero, shown in equation 3.24, while the loading occurs along one dimension.

$$\epsilon_x \neq 0, \epsilon_y = \epsilon_z = 0 \tag{3.24}$$

The stress in the x direction is calculated through the equation 3.25, while the stresses in the y and z directions are equal to each other and are calculated through equation 3.26,

$$\sigma_x = M\epsilon_x \tag{3.25}$$

$$\bar{\sigma} = \sigma_{y,z} = \frac{M\nu}{1-\nu}\epsilon_x = \lambda\epsilon_x \tag{3.26}$$

where the parameter λ is referred to as Lame's first parameter and M is expressed in terms of Young modulus E and Poisson's ratio ν, according to the equation 3.27.

$$M = \frac{E(1-\nu)}{(1-\nu)(1-2\nu)} \tag{3.27}$$

This condition is not commonly seen in classical mechanics as it demands very high strain-rate loading or a condition of high confinement. Under this high strain rate, the material tends to react like a fluid, and for a short period of time, as the shock wave propagates, the material remains within uniaxial strain until a rarefaction wave relieves it. Uniaxial stress, hydrostatic loading, and uniaxial strain stress-strain conditions are shown in Figure 3.39 [31].

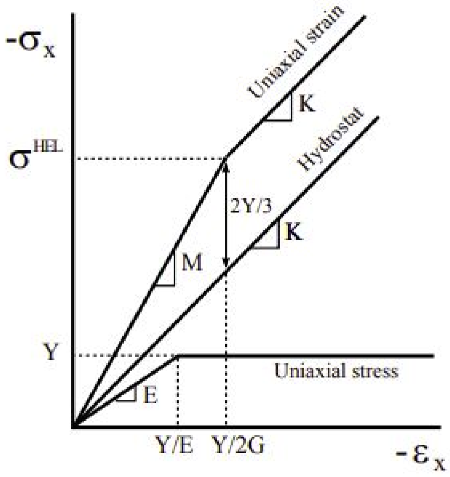

Figure 3.39. Uniaxial Strain vs. Hydrostatic Compression vs. Uniaxial Stress of Elastic-Perfectly Plastic Material. Source: [31].

The yield point in the uniaxial strain condition is calculated using the Von-Mises Criterion following the equation 3.28 [31],

$$\sigma_x - \bar{\sigma} = Y \tag{3.28}$$

where Y is the yield stress under uniaxial stress conditions. Using this criterion of equation

3.28, the strain in the yield point under uniaxial strain is defined by the equation 3.29, 3.28,

$$\epsilon_x^{yield} = \frac{Y}{2G} \tag{3.29}$$

where G is the Shear modulus, and the corresponding stress at this point is called Hugoniot Elastic Limit HEL and is given by the equation 3.30,

$$\sigma^{HEL} = \left(\frac{K}{2G} + \frac{2}{3}\right)Y \tag{3.30}$$

where K is the Bulk modulus. In a uniaxial stress condition for an elastic perfectly plastic material, once the stress reaches the yield point, it remains there while the material continues to deform. However, on the uniaxial strain condition, once the material reaches the yield point, the $\bar{\sigma}$ increases along with σ_x, thus the material can maintain the yield condition. It moves parallel to the hydrostat curve by a shift of $\frac{2Y}{3}$, while the σ_x increases, according to the equation 3.31,

$$\sigma_x^p = K\epsilon_x + \frac{2Y}{3} \tag{3.31}$$

considering that at this regime the Shear modulus G is equal to 0, as the material is treated as fluid. In most metals and ceramics the Y is in order of a few hundred MPa. So, dealing with stresses much larger than Y, the response of the material can be simulated like a fluid's one, ignoring any material strength or shear stress loading [31]. This is a very important point in shock physics, while the high-velocity impacts bring the material under such loading conditions that reach a few tens of GPa due to the shock waves generated, and a fluid-like response is a good approximation [31].

3.5.2 Shock Waves

High-velocity impacts are characterized by high strain rates that reach the order of $10^3 - 10^8\ sec^{-1}$ [31]. Typically, during high strain rates, shock waves are generated. Shock waves form a discontinuous jump as a compression discontinuity within the material. When a dynamic stress condition is imparted onto a target, exceeding the HEL, the load propagates through the material as either a single shock wave or a two-part shock wave incorporating a higher velocity elastic wave followed by a higher pressure shock wave or an overdriven shock which proceeds at a lower velocity than the elastic wave. The elastic wave travels typically faster than the overdriven shock waves, provided that the slope of the Rayleigh line does not exceed the slope of the elastic modulus. The elastic waves are divided into two waves, the longitudinal and the shear. The longitudinal waves are faster than the shear wave. Their velocity is given by the equation 3.32 [31].

$$C_l = \sqrt{\frac{\lambda + 2G}{\rho}} = \sqrt{\frac{M}{\rho}} \tag{3.32}$$

where ρ is the density. The plastic wave follows the elastic waves and its velocity is calculated from the equation 3.33,

$$C_{pl} = \sqrt{\frac{d\sigma/d\epsilon}{\rho}} \tag{3.33}$$

where $d\sigma/d\epsilon$ is the slope in the plastic regime area. A characteristic graph of the Shock wave pressure profile is shown in Figure 3.40.

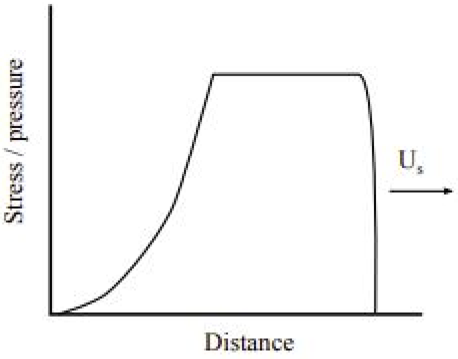

Figure 3.40. Shock Wave Pressure Profile. Source: [31].

The shock wave is a disturbance in the material that travels at supersonic speeds relative to the material in front of the shock wave in the uncompressed material and at subsonic speeds within the compressed region (higher compressed material enables a higher elastic/shock velocity) [31]. The width of the shock front depends on the material properties as well as other factors, including porosity and heterogeneity. The changes in material properties from an incident shock wave take place in less than 0.1 sec, and the shock front is followed by a constant pressure profile. The shock pressure is relieved through a rarefaction/relief wave.

The front peak of the rarefaction/relief wave travels faster than the shock wave. The rarefaction/relief wave fans out as it propagates through the shock wave. The rarefaction/relief wave reduces shocked material pressure condition over a longer period of time. A representation of this is shown in Figure 3.41 [31].

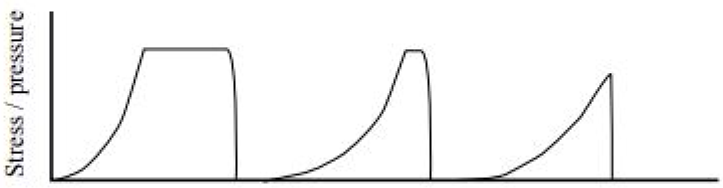

Figure 3.41. Rarefaction Wave Overtaking the Shock Wave. Source: [31].

3.5.3 Rankine-Hugoniot Jump Equations

Shock waves increase the pressure within a material, as well as its density and internal energy. Beyond the shock wave, a particle velocity is imparted. The condition of the material impacted by a planar 1D shock wave is characterized by Rankine-Hugoniot 1D jump equations and defined by the conservation of mass, momentum, and energy across the shock front inside the material [31]. When the shock front crosses the material, considering mass is passing in and out of a Lagrangian frame of reference, the mass conservation law is presented with the equation 3.34,

$$\rho_o A U_s dt = \rho A(U_s - u_p)dt \tag{3.34}$$

where ρ_o and ρ are the densities in front and behind the front, whereas U_s represents the shock velocity, u_p is the particle velocity, and A is a reference cross-sectional area. The conservation of momentum, equation 3.35, is calculated through the conservation of momentum of material that the shock wave passes through [31].

$$PAdt = m\Delta u = (\rho_o A U_s dt)u_p \tag{3.35}$$

Lastly, energy conservation across the shock front is described by the equation 3.36

$$\underbrace{PAu_pdt}_{\text{Force Work}} = \underbrace{\rho_o U_s Adt(E - E_o)}_{\text{Internal Energy}} + \underbrace{\frac{1}{2}(\rho_o U_s Adt)u_p^2}_{\text{Kinetic Energy}} \tag{3.36}$$

A key parameter in shock physics is the shock impedance Z, calculated by the equation 3.37.

$$Z = \rho_o U_s \tag{3.37}$$

The shock impedance determines how a shock wave responds at a material interface between two materials. The transmitted and reflected waves are defined by the relative change in impedance. An incident shock wave at an interface with a higher impedance material generates both a transmitted and reflected shock wave of higher pressure (equation 3.38) [31].

$$P = Zu_p \tag{3.38}$$

The Hugoniot EoS relates the shock velocity U_s to the particle velocity u_p. An example of a linear Hugoniot EoS is shown in equation 3.39.

$$U_s = A + bu_p \tag{3.39}$$

The value A is the sound velocity of the target material, while b is a material characteristic factor that multiplies the particle velocity. As the particle velocity approaches zero, the shock velocity becomes the elastic wave velocity. The Hugoniot EoS is determined by a polynomial fit between the pressure and the particle velocity of several 1D planar shock experiments. For many metals, the material response can be linear shown by the equation 3.39 [31]. Figure 3.42 depicts the Hugoniot EoS for different materials. One of its representations is in the $P - u_p$ domain, while it can be also met in the $P - v$ domain, where v is the specific volume.

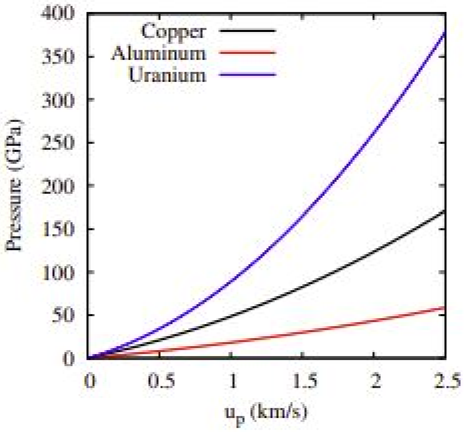

Figure 3.42. Hugoniot Curves in $P - u_p$ Domain. Source: [31].

While the Hugoniot curve represents the pressure vs. the particle velocity state of a material, it is not a compression path that is followed during the shock wave crossing. Rather, each point of the curve represents the end-state pressure that is achieved in the material for a given shock wave. For lower pressures, the Hugoniot curve closely resembles an isentrope (accurate to 3rd order in a power series expansion).

When a projectile/impactor impacts a target, the target material jumps to the new pressure state. The straight line path is called the Rayleigh line, shown in figure 3.43, bringing the target material to its new shocked state. This line is following the equation 3.38 where the slope is the shock impedance of the target. This point is the only point that satisfies the conservation equations and determines the material state after the shock wave crossing. Multiple impacts at different impact pressures are required to enable the construction of a Hugoniot curve [31].

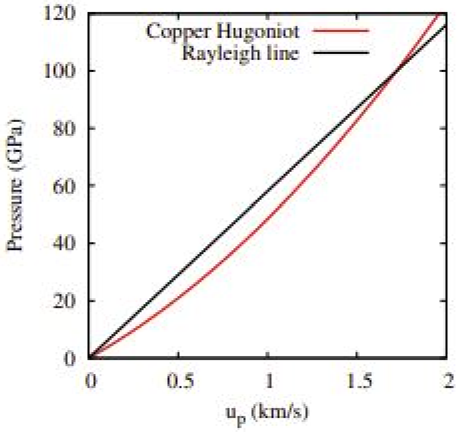

Figure 3.43. Hugoniot and Rayleigh Line Intersection. Source: [31].

3.5.4 Impedance Matching

Impedance matching enables the determination of both pressures and particle velocities at an interface. In Figure 3.44, an incident shock wave, within material I, reaches the interface between material I and II. Material II is at a higher impedance than material I. Within figure 3.44 the shock waves are represented by solid lines, while the material interface is shown with dashed lines, in the $x - t$ domain.

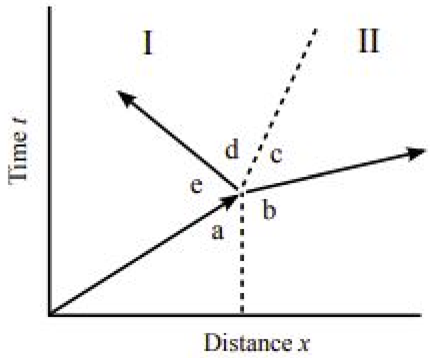

Figure 3.44. Distance vs. Time Shock Striking Propagation. Source: [31].

Starting at time zero, the shock wave is moving towards the interface at a constant velocity, while the interface is not moving and not sensing that is going to be hit by this. When it does hit the interface, the shock wave is transmitted and reflected back in different velocities, shown by the slopes in the graph, and the interface also starts moving with the particle velocity. To move to the $P - u_p$ domain shown in Figure 3.45, the pressure and the particle velocity are continuous at each line in the graph.

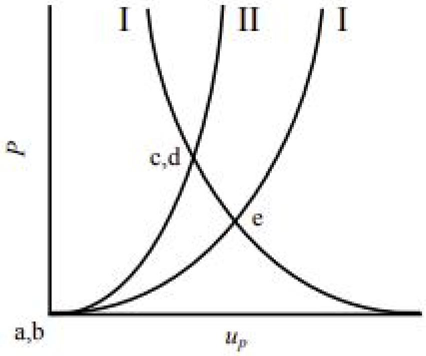

Figure 3.45. Impedance Matching Graph. Source: [31].

In regions a and b, materials I and II are at an initial pressure as shown in figure 3.45. After the shock, both materials jump to state "c". Specifically, material II has higher shock impedance; otherwise, the shock wave could not reflect back at material I as a shock wave but as a rarefaction wave. In Figure 3.45, the state "c" can be determined by drawing the Hugoniot curves for each material individually that intersect at the state "c". The difference is that for material I, the Hugoniot is facing to the left, mirroring the initial curve starting from b. This is because material I already has a particle velocity as it moves towards material II before the impact.

The impact interface shares the same pressure and particle velocity [31]. The key for interpreting Figures 3.44 and 3.45 is to understand that d and c represent the shock waves in two different materials, but they are identical. So the impedance match point of material I impacting material II with pressure p determines the particle velocity to satisfy the equations of state for both materials. Thus, the impedance matching point is the intersection of the right-facing material II curve and the left-facing material I curve [31]. The pressure at the impedance matching point for material I is given by the equation 3.40,

$$P = \rho_{oI}[A_I + b_I(u_i - u_p)](u_i - u_p) \tag{3.40}$$

where u_i is the velocity just before the impact and is the intersection of material I curve with the horizontal axis to the right in Figure 3.45. The relative equation for the target material II is given as:

$$P = \rho_{oII}[A_{II} + b_{II}u_p]u_p \tag{3.41}$$

Another condition occurs when the reflected shock wave into a material hits the free-back surface of the material again resulting in an impedance mismatch. This time, because the air has almost negligible shock impedance, the shock wave reflects back into the material as a rarefaction wave, trying to bring the pressure back to zero, as shown in Figure 3.46. The rarefaction wave is divided into smaller waves each one traveling at a constant different velocity, evolving in time and decompressing the material initial state [31].

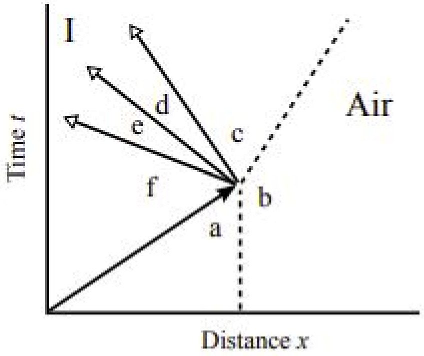

Figure 3.46. Shock Wave and Free Surface Impedance Matching. Source: [31].

The pressure at the free surface is equal to zero and the rarefaction wave follows an isentropic curve to bring the pressure from the compressed state to zero point. It can be considered that the rarefaction wave follows the Hugoniot curve only for metals, as it is almost identical to an isentrope [31].

Following the same analysis used for Figure 3.44, the free surface region c should be identical to region b. Thus, the pressure is zero there, but the free surface is already moving. So for material I, the left-facing Hugoniot curve intersects the horizontal axis at the point of $2u_p$, considering the symmetry of the problem [31].

3.6 Application of Theory to the Experiment

Two different test configurations were performed to obtain different shock wave measurements. Measurements include shock impact pressure and elastic precursor waves. Each target design enables proper measurement of the required shock. Primary measurements incorporate Lithium Fluoride (LiF) windows and PDV to enable interface pressure measurements.

3.6.1 Measuring the HEL

In the Elastic Precursor configuration, the elastic precursor is studied as an indication of a possible amorphous shear band failure in B_4C. For lower Poisson's ratio materials, an elastic precursor can be observed. To observe the elastic wave, an experiment must enable a travel distance to enable the elastic wave to lead the shock wave. In this type of experiment, a copper disk impactor impacts the B_4C back face. The front face of the B_4C surface is mounted to the back surface of a LiF window. The back surface of the LiF is sputter-coated with a reflective metal to enable the back reflection of the incident PDV laser beam. The LiF transparency enables the particle velocity between the B_4C and LiF to be measured. The general graphical representation of this configuration is shown in Figure 3.47.

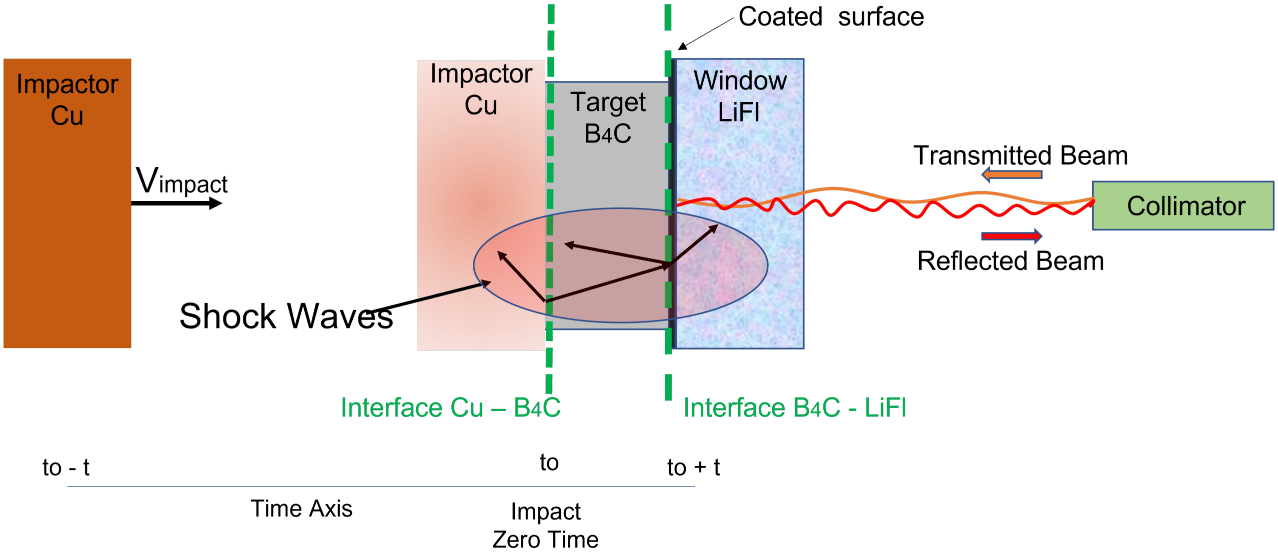

Figure 3.47. Target Configuration Measuring the HEL

At $t_o = 0$, the Copper (Cu) impactor hits the B_4C target, and two shock waves are generated, traveling both into the Cu impactor and B_4C target, Figure 3.47. Within the B_4C target, over a short distance, the elastic wave will lead the generated shock wave. The particle velocity that is measured, by the PDV at the B_4C-LiF interface, includes both the elastic wave followed by the shock velocity. Due to reflections of the elastic wave in B_4C, the magnitude of the shock pressure is altered due to the superposition of the reflected elastic wave within the B_4C.

The second configuration enables the measurement of the shock impact pressure. In this configuration, the B_4C impactor impacts the back surface of a LiF window. The back surface of LiF is also coated with a reflective surface. This enables PDV to measure the particle velocity at the interface (Figure 3.48).

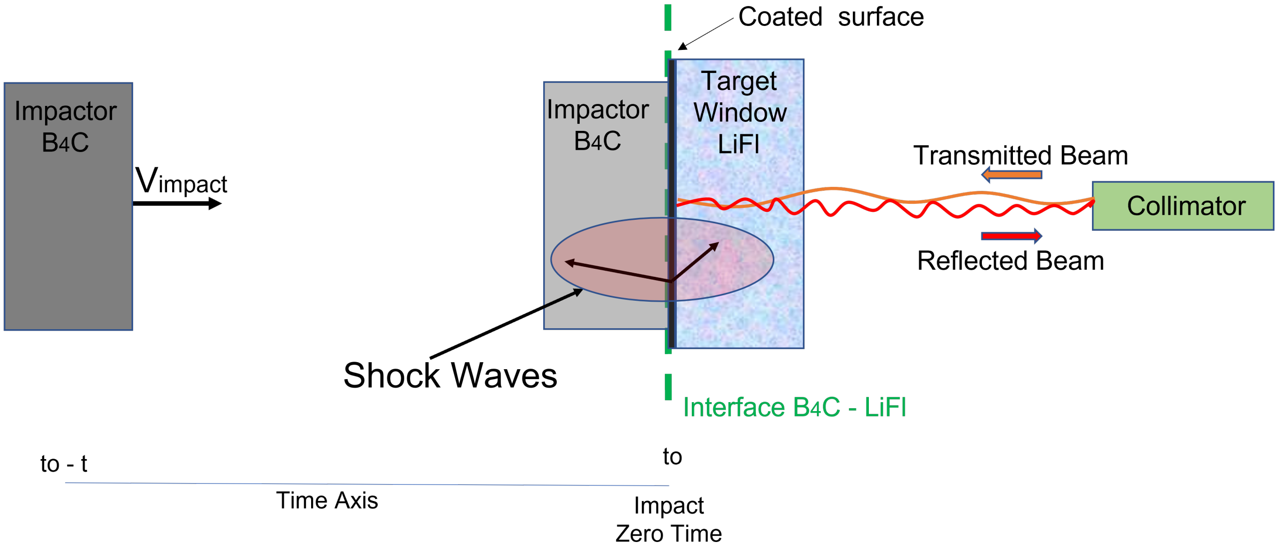

Figure 3.48. Target Configuration Measuring the Plastic Wave

The impact pressure can be determined by measuring the particle velocity u_p at the B_4C-LiF interface using the B_4C as the impactor (configuration 2) and applying the impedance matching. The pressure at the interface is the same regarding B_4C and LiF, so it is enough to use one of the materials EoS to determine it. The LiF EoS is chosen as it is exclusively defined by the equation 3.42 [32],

$$P = 2638(5201 + 1.323 * u_p)u_p \tag{3.42}$$

where $\rho = 2638\, kg/m^3$ and $A = 5201\, m/s$. The pressure (in units of Pa) calculated is the HEL of B_4C, as it is the pressure that the material experiences if it is crossed by an elastic wave.

3.6.2 Measuring $C_{elastic}$ and $C_{plastic}$

In the third configuration, the impactor is a Cu disk, hitting the back surface of B_4C. The difference in this configuration is that the PDV measures the free surface velocity of B_4C. As was mentioned in section 3.5.4, the free surface velocity driven by a shock wave corresponds to double the particle velocity. PDV measures the free surface velocity. This technique, similar to the 2nd configuration, can only enable a qualitative analysis of the propagated wave (Figure 3.49).

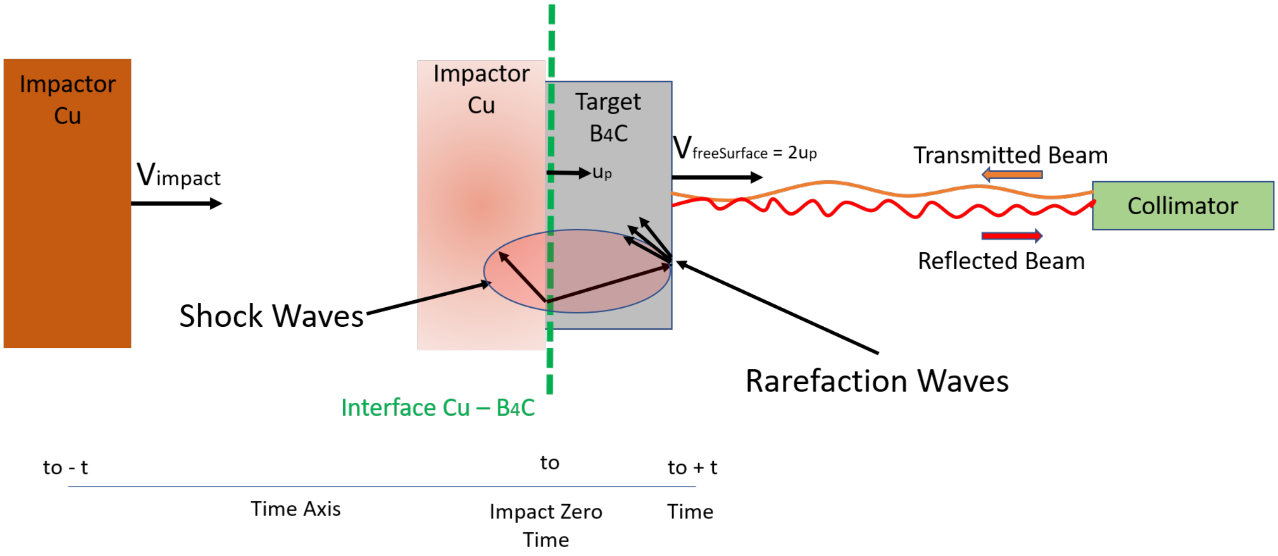

Figure 3.49. Target Configuration Measuring Both Elastic and Plastic Wave

THIS PAGE INTENTIONALLY LEFT BLANK

CHAPTER 4:
Results

4.1 X-Ray Diffraction Measurements

Table 4.1 presents the crystallite sizes and the volume changes of the XRD results. The HEBM of B_4C increased the crystallite size by 0.26%. An even greater change was observed in the Zr: 1 atom enriched sample where the volume increased by 1.26%. In the Si: 1 atom though, no significant change in the lattice parameters was observed (-0.02%).

Table 4.1. B_4C Alloy XRD Data

Lattice Parameters					
Alloy Type	a(A)	b(A)	c(A)	V(A^3)	$\Delta V\%$
B_4C	5.5995	5.5995	12.071	327.77	-
B_4C:HEBM	5.604	5.604	12.0833	328.63	0.2623
B_4C:Si:1at	5.6	5.6	12.06	327.7	-0.02136
B_4C:Zr:1at	5.616	5.616	12.152	331.9	1.26

The graphs of 2θ XRD pattern, for each of the four powders sampled, are shown below. The four ceramic powders are superimposed onto one graph to observe any shifts in the characteristic peaks of B_4C. The Si and Zr samples ball milled into B_4C in the superimposed graph are shifted vertically with respect to the origin so as to be easily compared.

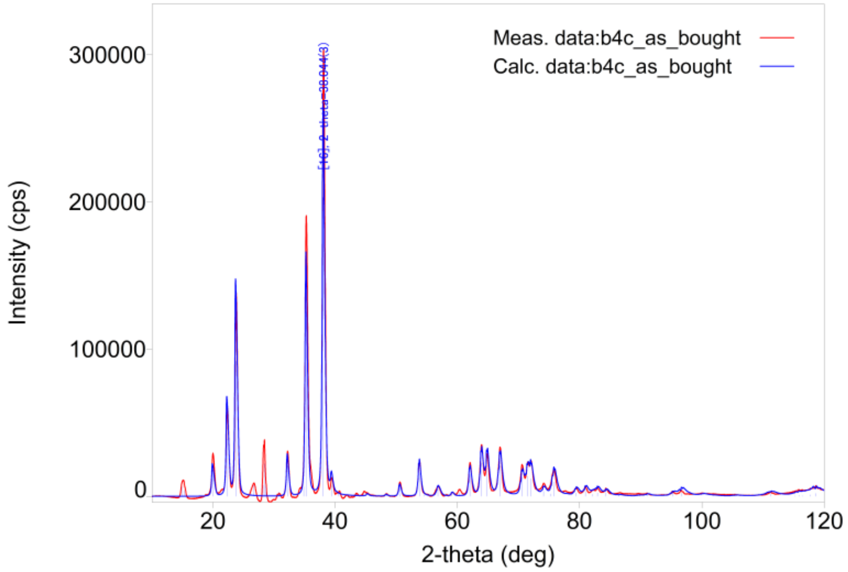

Figure 4.1. XRD Data of B_4C: "as bought"

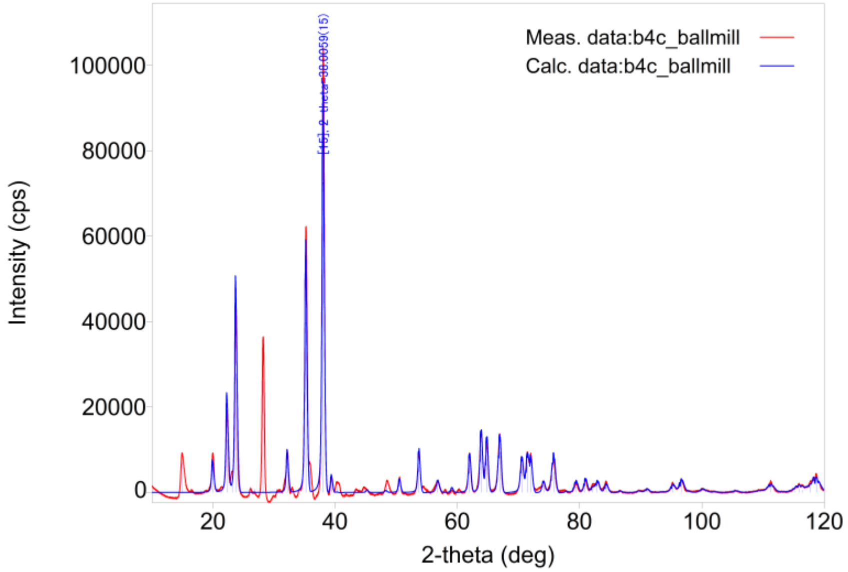

Figure 4.2. XRD Data of B_4C:HEBM

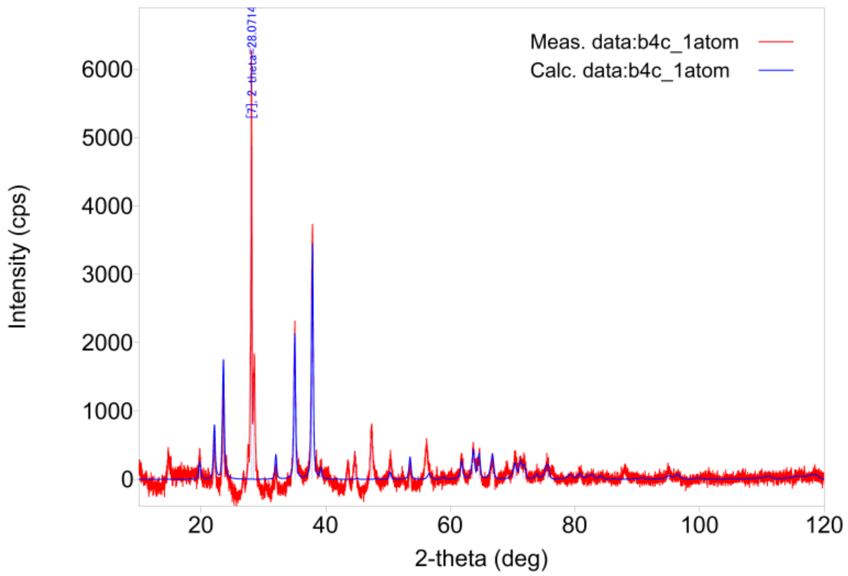

Figure 4.3. XRD Data of B_4C: Si 1 Atom

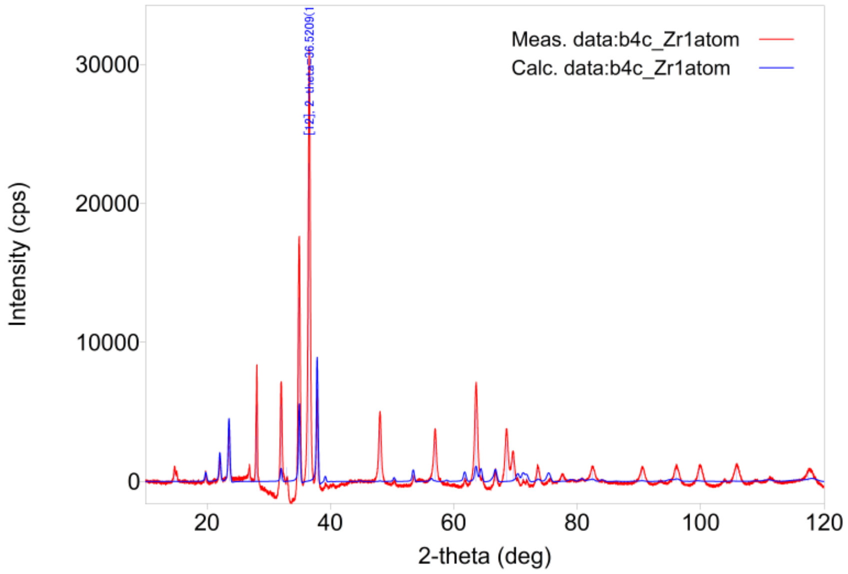

Figure 4.4. XRD Data of B_4C: Zr 1 Atom

By superposing all the XRD plots into one (Figure 4.5), the samples' XRD footprints show variations from the initial B_4C XRD curve peaks (blue line).

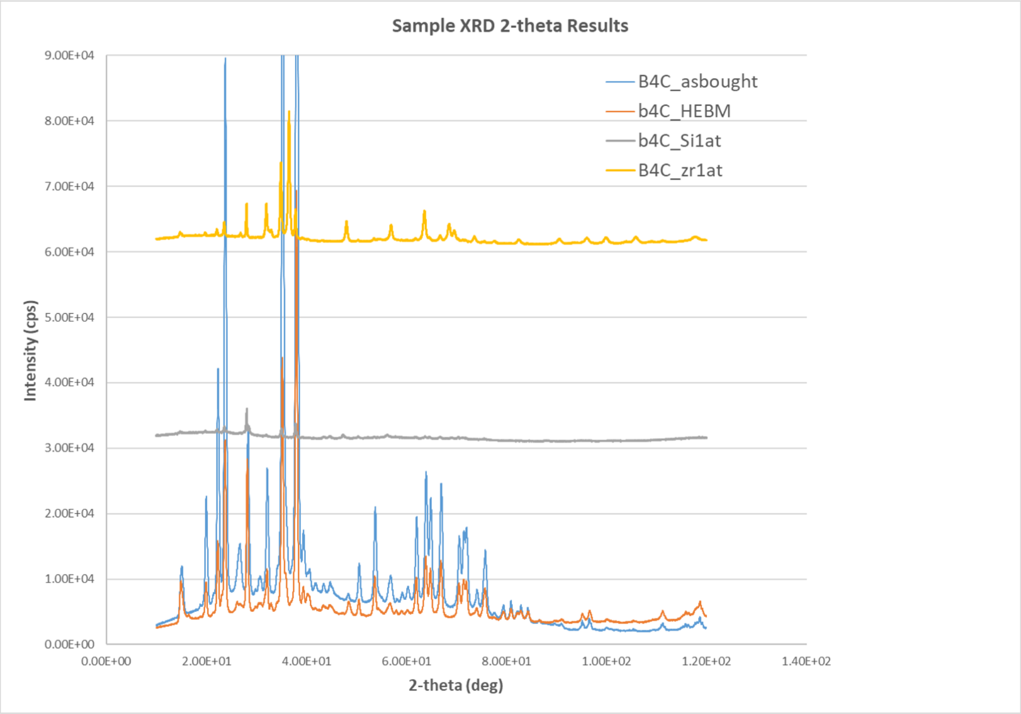

Figure 4.5. XRD Sample Data

B_4C, B_4C:HEBM, and B_4C: Si are almost identical as the peaks coincide. B_4C: Zr 1 atom though (yellow line), is shifted to the left. This reduction in 2θ angle indicates an expansion to the unit cell of B_4C: Zr 1 atom.

4.2 SEM Observations

The presented four powder samples include: B_4C "as bought", HEBM B_4C, B_4C: Si 1 atom, and B_4C: Zr 1 atom. The magnification of the tested samples varied from $500x$ and 10^4x. Within figure 4.6 the B_4C "as bought" particle size was observed to be $\sim 100\,\mu m$. The HEBM B_4C sample (figure 4.6) showed a 70% reduction in particle size at $\sim 30\,\mu m$. The same was also observed for the samples of B_4C: Si 1 atom and B_4C: Zr 1 atom. This reduction in particle size indicates the HEBM impact on the initial powder which in turn, it is expected to be the reason for high-quality ceramic with increased hardness and density close to the TMD.

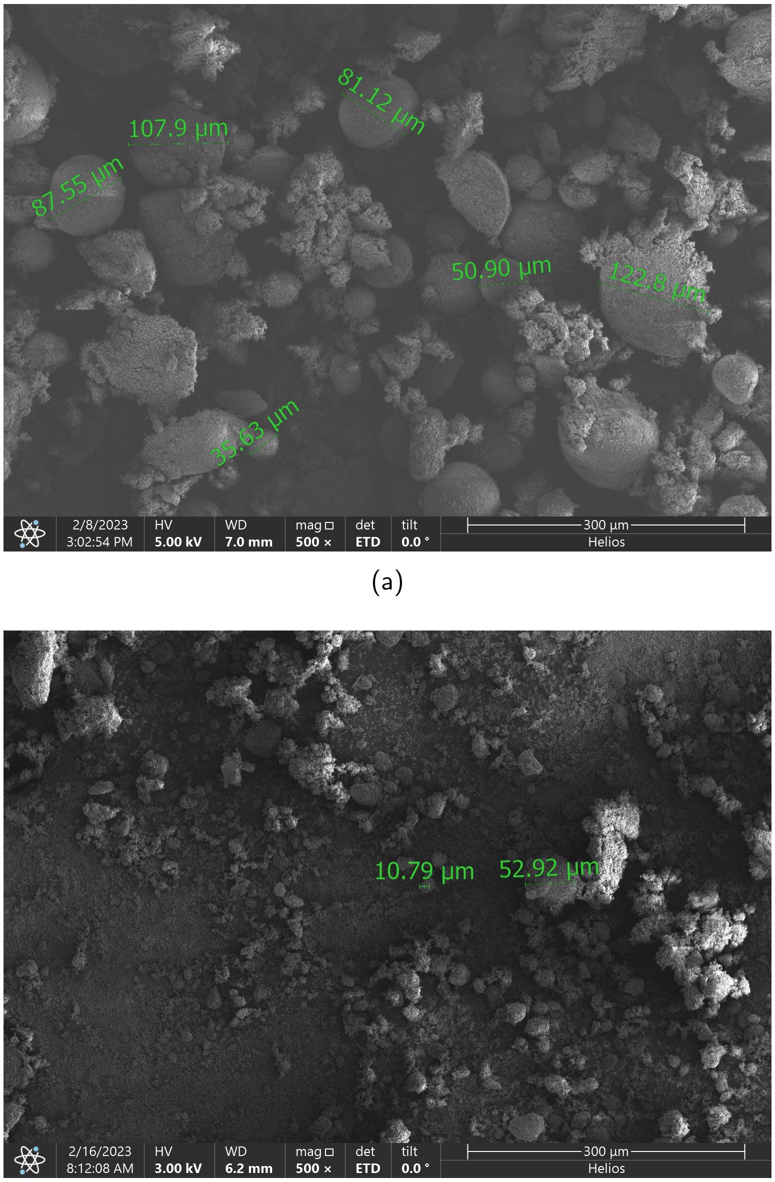

(a)

(b)

Figure 4.6. (a) B_4C "as bought" Powder at 500x Magnification (b) B_4C:HEBM Powder at 500x Magnification

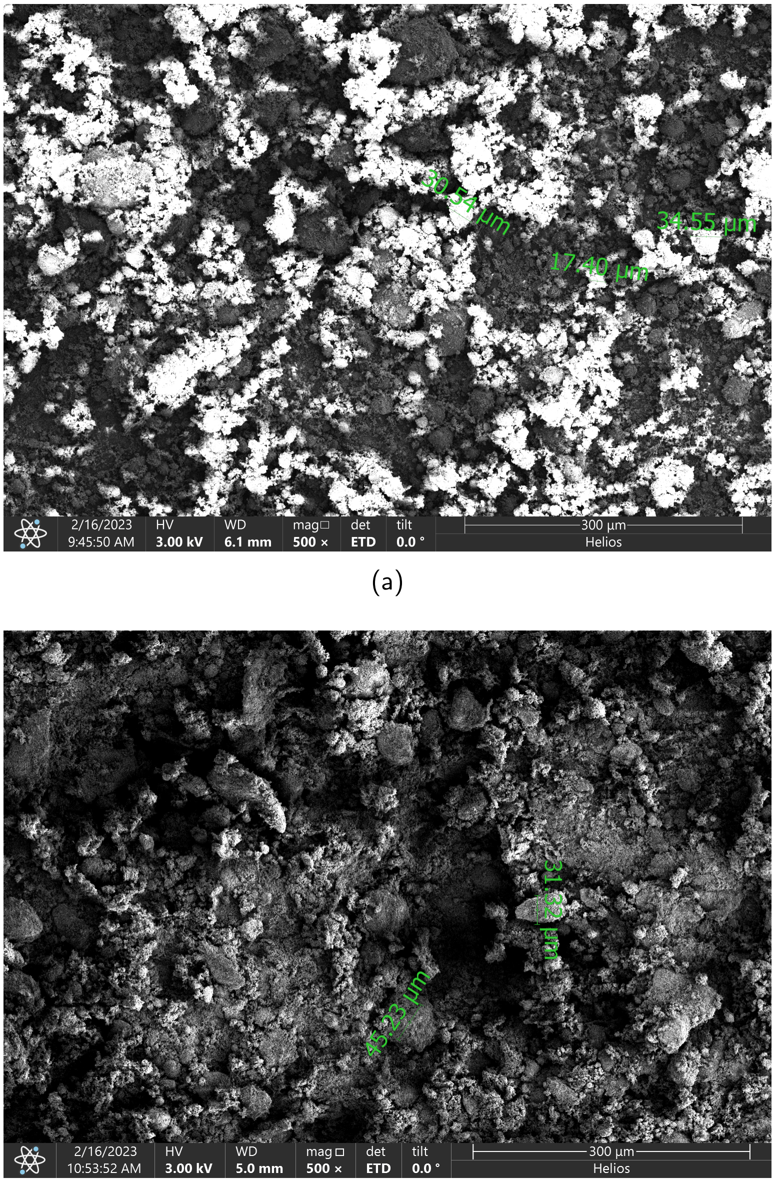

(a)

(b)

Figure 4.7. (a) B_4C:Si Powder at 500x Magnification (b) B_4C:Zr Powder at 500x Magnification

Further magnification of 10^4, shows finer structures related to the correlation to the HEBM.

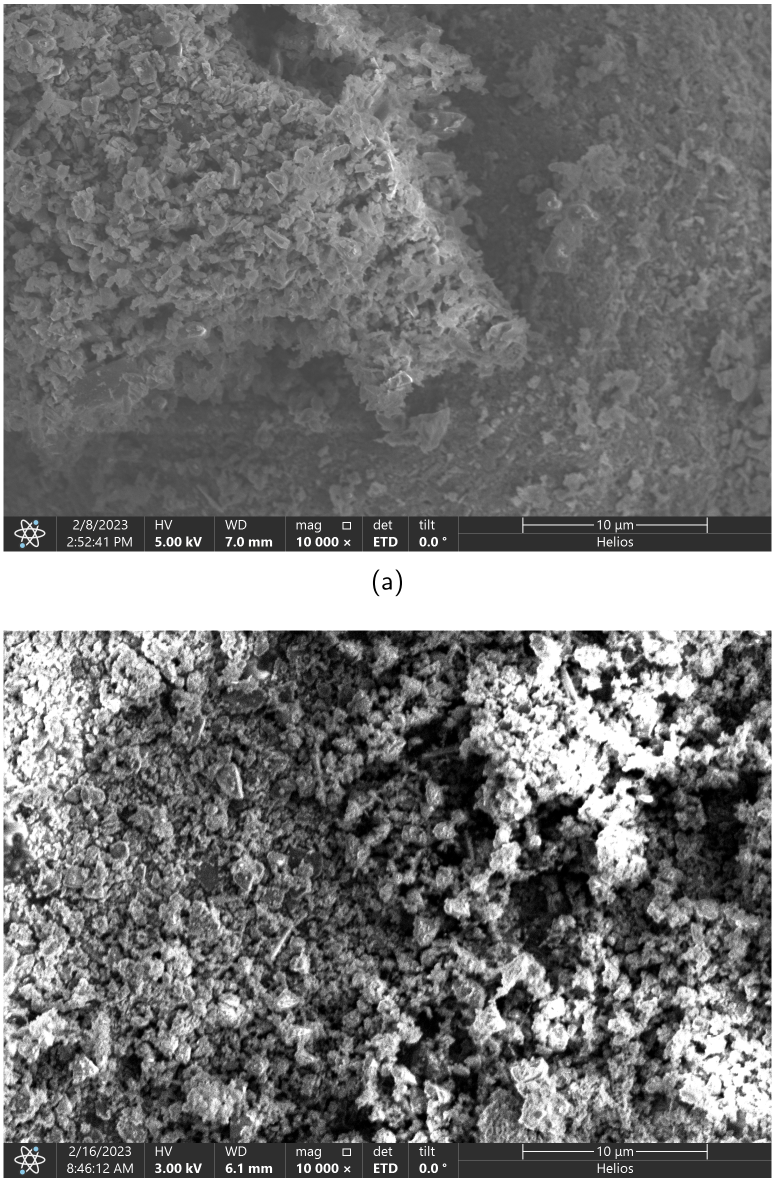

(b)

Figure 4.8. (a) B_4C "as bought" Powder at 10000x Magnification (b) B_4C:HEBM Powder at 10000x Magnification

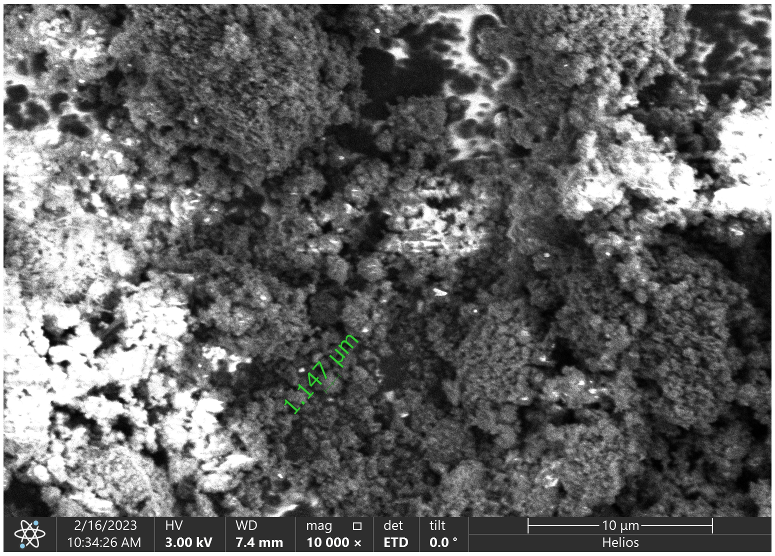

(a)

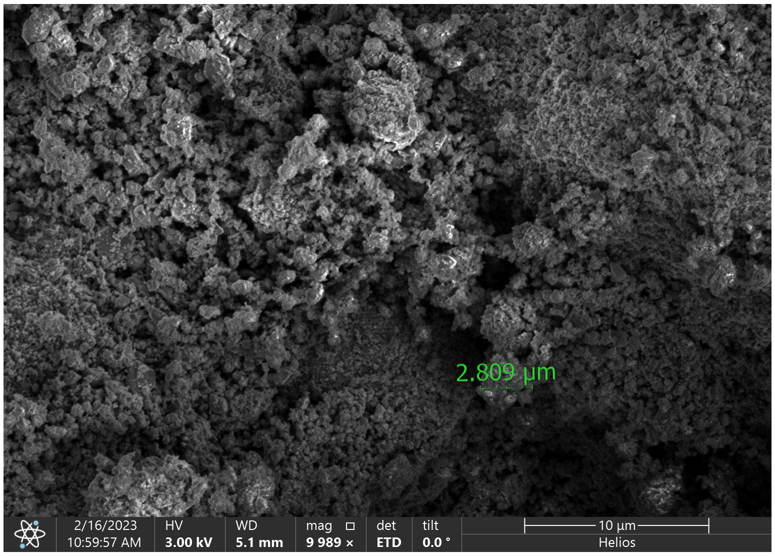

(b)

Figure 4.9. (a) B_4C:Si Powder at 10000x Magnification (b) B_4C:Zr Powder at 10000x Magnification

The HEBM clearly affected the particle size reduction. The HEBM powders enabled smaller particles as compared to the B_4C “as bought” powder sample.

4.3 Density and Hardness Test Results

Any armor ceramic should be at least 97% of the TMD value to enable the required performance. Table 4.2 shows the densities of the B_4C ceramic disks, compared to previous work [22].

Table 4.2. B_4C Alloy Densities

Measured Densities (kg/m^3)		
Alloy Type	TMD	Measured
B_4C	2520	2500
B_4C:HEBM	2520	2471
B_4C:Si, 1/2at	2560	2224
B_4C:Si, 1at	2773	2184
B_4C:Zr, 1at	3733	3190

B_4C and B_4C:HEBM densities were near the TMD for B_4C. A larger reduction in density was observed though for both Si samples of (1/2 atom and 1 atom). As the hot press temperature and pressure were optimized for B_4C: "as bought" further pressing studies may improve the hot pressed densities of the B_4C powders with elemental inclusions.

Table 4.3 presents the Vickers Hardness of the 5 different samples tested. The hardness of the B_4C:HEBM demonstrates a hardness similar to the B_4C: "as bought" hot-pressed ceramic. The Si enriched samples, showed different values. The $1/2$ atom inclusion was close to B_4C while the 1 atom presented a lower hardness. A possible explanation is the 1 atom inclusion enables more defects. The non-ideal hot-pressing assumption is also supported by the variation in the values of 1 atom of Zr inclusions. These samples showed an extremely large difference in hardness which may be correlated to the hot pressing technique.

Table 4.3. B_4C Alloys Vickers Hardness Test Results

Measured Vickers Hardness		
Alloy Type	sample	sample
B_4C	3475	4925
B_4C:HEBM	3374	
B_4C:Si, 1/2at	3237	
B_4C:Si, 1at	2495	
B_4C:Zr, 1at	4011	2678

4.4 Experimental Process

In the shock impact studies of OFHC Cu impacting B_4C ceramics, the precursor elastic wave is investigated to understand the response of B_4C and variants with elemental inclusions of Si and Zr. Previous observations have shown that impacts above the HEL, for B_4C, demonstrate a surface softening within the precursor elastic wave due to the amorphous shear band failure.

The PDV measurements enable the analysis of the precursor elastic wave as a particle velocity vs. time displaying both the precursor elastic wave and the shock wave.

In addition to the investigation of the elastic precursor, two tests were performed to measure the impact pressure following the Rayliegh line of the Hugoniot for both B_4C: "as bought" and a B_4C:Zr applied as the impactor impacting a LiF target window. This configuration enabled the direct impact pressure. Measurement of the elastic precursor wave was presented in section 4.4.3, where an OFHC copper impactor hits the ceramic target backed by a LiF target window.

4.4.1 Impact Planarity Measurements

All of the shots were planar with respect to the relative orientation of the projectile to the target. For an impact to be considered planar, the front face of the projectile has to impact the back face of the target with an angle smaller than 1^o. Below is presented the angle computation of one elastic precursor wave measurement shot.

The initial projectile velocity, exactly before the impact, was $V_p = 1875\, m/s$. Figure 4.10 shows the 4-pin timestamps. Based on the vertical peak, each pin's timestamp was extracted.

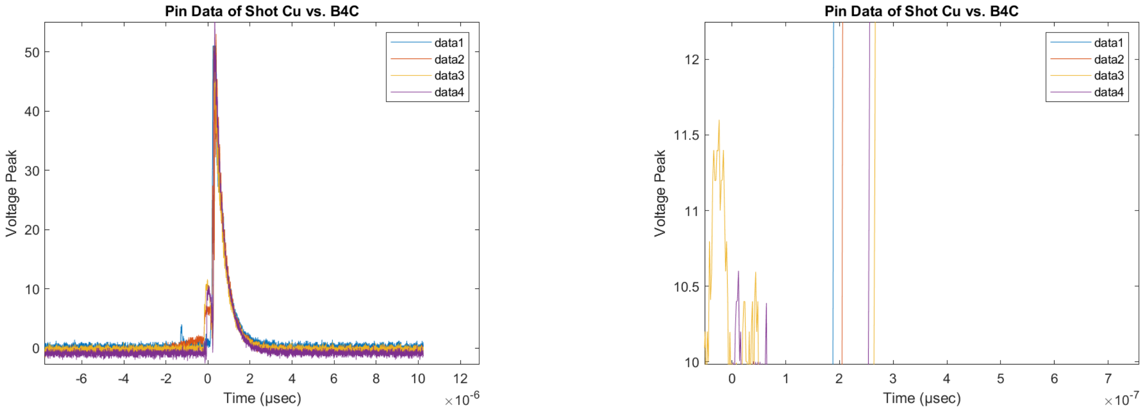

(a) (b)

Figure 4.10. (a) Pin Timestamps Graph (b) Pin Timestamps Graph Zoomed In

The impact time points are:

$$\begin{aligned} time_{pin1} &= 0.19\, \mu sec \\ time_{pin2} &= 0.208\, \mu sec \\ time_{pin3} &= 0.268\, \mu sec \\ time_{pin4} &= 0.258\, \mu sec \end{aligned} \tag{4.1}$$

Based on those timestamps, the vertical magnitudes of the blue and orange vectors in Figure 4.11 are calculated using equation 3.14.

$$\begin{aligned} dz_{31} &= V_{impactor} * (time_3 - time_1) = 1.4625 * (1e - 4)m \\ dz_{42} &= V_{impactor} * (time_4 - time_2) = 0.9375 * (1e - 4)m \end{aligned} \tag{4.2}$$

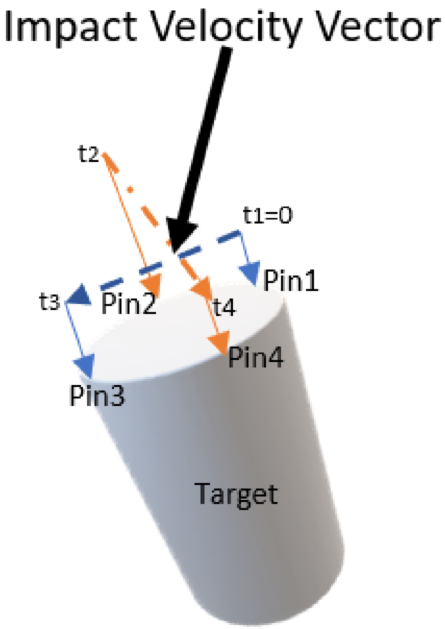

Figure 4.11. Impact Planarity Vector Representation

The vector magnitudes by using the target surface as the XY plane are:

$$\begin{aligned} Vector_{blue}^{13} &= [0.034, 0, dz_{31}] \\ Vector_{orange}^{24} &= [0, 0.034, dz_{42}] \end{aligned} \tag{4.3}$$

By taking their cross product, the V_{Impact} vector is calculated as:

$$\overrightarrow{V_{imp}} = \begin{vmatrix} \hat{x} & \hat{y} & \hat{z} \\ 0.034 & 0 & -dz_{31} \\ 0 & 0.034 & -dz_{42} \end{vmatrix} = [0, 0, 0.0012] \tag{4.4}$$

Finally, the angle θ_{imp} between the normal to the impact surface and the cross-product V_{imp} is calculated from the equation 3.19.

$$\cos(\theta_{imp}) = \frac{\overrightarrow{V_{imp}}\vec{z}}{|V_{imp}||\vec{z}|} = 0.2924^{o} \tag{4.5}$$

4.4.2 Impact Pressure Experiments

Figure 4.12 presents the impact pressure of a B_4C "as bought" vs. a B_4C: Zr target. The pressure can be determined by using the EoS of LiF 3.42. At impact, B_4C experienced a 24 GPa pressure, while B_4C: Zr experienced a 36.4 GPa pressure. The pre-impact velocities were 1525 m/s for the B_4C and 2076 m/s for the B_4C: Zr. It is clear that the targets jumped directly to a compressed state beyond the HEL of $\sim 20\,Gpa$. Because of the impact velocity differences, a conclusion on how the Zr inclusion affects the impact behavior cannot be determined.

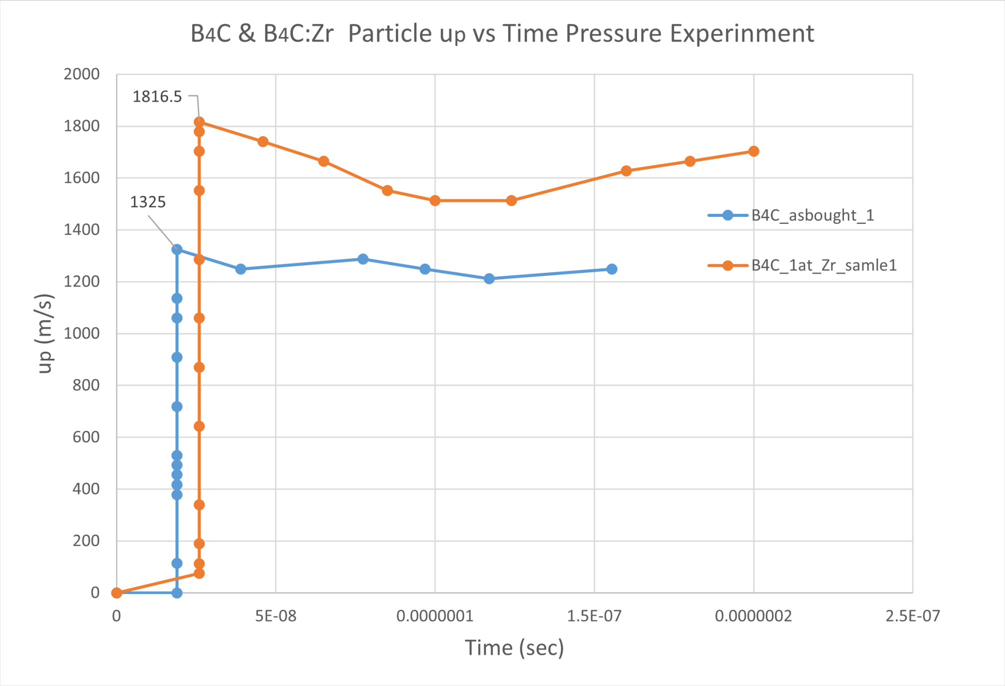

Figure 4.12. Impact Pressure Graph of Particle Velocity vs. Time

4.4.3 Elastic Precursor Experiments

Figure 4.13 shows the HEL and the post-yielding behavior of two B_4C targets made of "as bought" and "HEBM" powders. The configuration incorporating elastic wave studies used an OFHC Cu impactor and a two-body (B_4C/B_4C variant target- backed by a LiF window). For many materials that have a lower Poisson's ratio, an elastic precursor wave can be observed. The elastic precursor wave can be used to determine if post-yield softening occurs within B_4C.

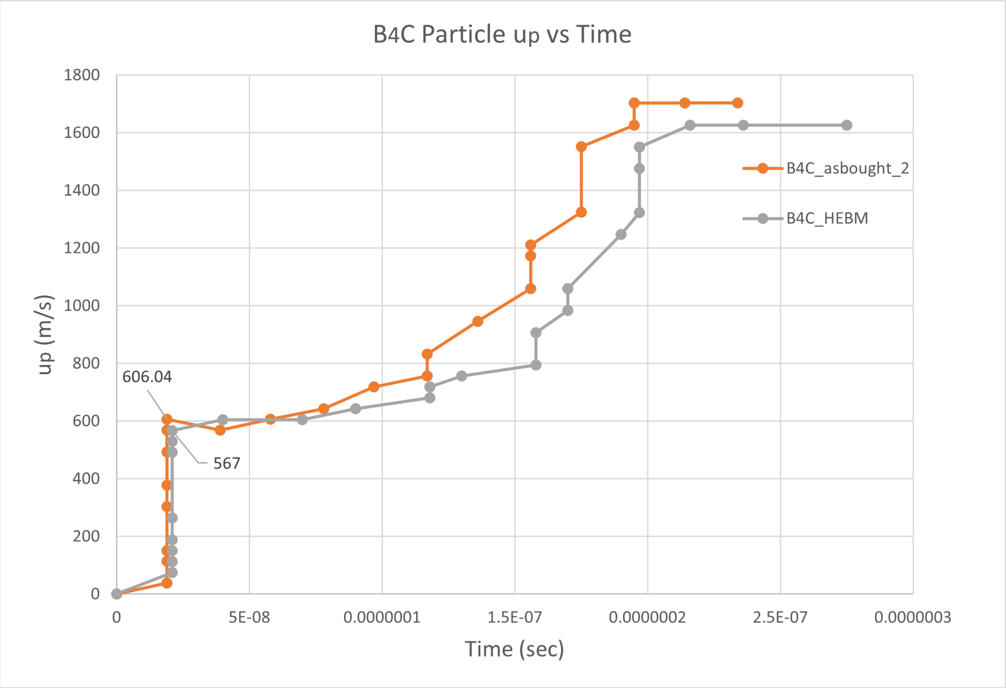

Figure 4.13. B_4C "as bought" and HEBM Elastic Precursor Waves

B_4C sample showed a HEL of 9.6 GPa at $u_p =\sim 606\,m/s$, while B_4C: HEBM showed a HEL of 8.9 GPa at $u_p = 567\,m/s$. Considering that the impact velocities for these experiments were 1875 m/s for B_4C and 1992 m/s for B_4C: HEBM, it can be assumed that the two samples behaved similarly. The HEBM of B_4C powder, from the elastic precursor, did not appear to improve the HEL based on a performance increase from the Hall Petch Effect where grain sizes were reduced.

Figure 4.14 shows the response of elementally included materials within B_4C through HEBM. The three targets presented include two B_4C: Si targets (1 and ½ Si atoms/unit cell) and one B_4C: Zr target (1 Zr atom per unit cell).

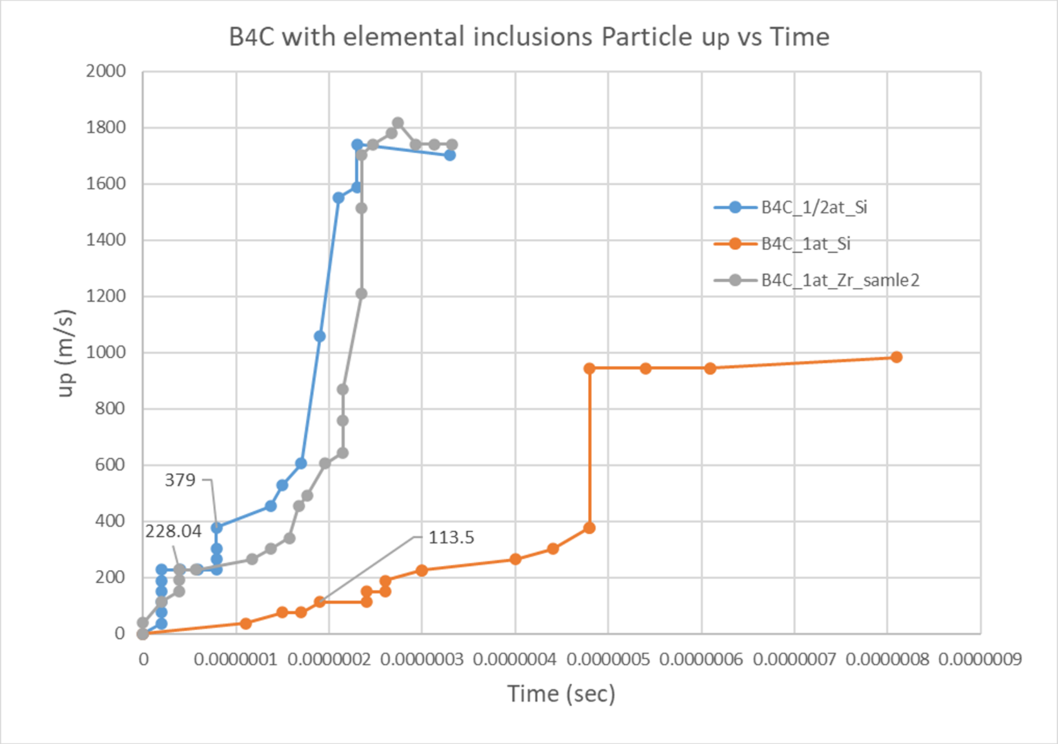

Figure 4.14. B_4C Elemental Inclusion Particle Velocity vs. Time

The 1/2 atom Si and the 1 atom Zr showed similar behavior regarding both the HEL and the post-yielding behavior. The 1 atom Si though, was quite different showing a lower elastic limit. A key parameter that can be observed is that all three targets showed a post-yield hardening. The HEL was 5.7 GPa for B_4C: Si (1/2 atom), 1.6 GPa for B_4C: Si (1 atom), and 3.3 Gpa for B_4C: Zr (1 atom). As the densities were lower than TMD for the elemental inclusions, the material strengths may have been reduced due to the selected hot-press parameters.

THIS PAGE INTENTIONALLY LEFT BLANK

CHAPTER 5:
Conclusion

The objective of this thesis was to examine how the placement of selected elemental inclusions within the B_4C lattice can alter the material strength of B_4C above the elastic limit. Primary studies investigated the post-yield-response of five different B_4C variations including B_4C "as bought", B_4C HEBM and three elemental inclusions using HEBM (1/2 Si, 1 Si, and 1 Zr atom) at impact pressures above the HEL of B_4C ($> 20\,Gpa$). A proposed theory for the observed post-yield softening of B_4C under high-impact pressures above the HEL supports that the B_4C unit cell ejects carbon atoms that enable the formation of shear bands sliding on the graphite layers of carbon atoms and resulting in the collapse of the B_4C unit cell. This thesis investigated the correlation between selected conditioning of the B_4C powders and the observance of post-yield softening.

DFT calculations suggest that for the most common B_4C polytype ($B_{11}C^P$-CBC) the preferred Si location is within the polar site of the icosahedron. This same site is the predicted location where C atoms are ejected and ultimately enabling the C atom chain to fail and form the amorphous shear bands. The placement of the Si atom within the polar site prevents C ejection from the B_4C unit cell resulting in the formation of amorphous shear bands.

The HEBM enables the capability to both reduce the grain size (Hall-Petch effect) and provide a low-temperature mechanism to place elemental inclusions within the B_4C unit cell. The energies achieved during the process are greater than the surface fracture energy, enabling the elemental inclusion into the original lattice of B_4C.

The powders were examined using XRD and SEM. The XRD showed that B_4C "as bought" and HEBM had almost identical 2θ peaks. For the elemental inclusions of Si 1 atom, no significant changes were observed. For 1 atom Zr, the lattice parameters changed significantly, increasing the unit cell volume and altering the diffraction peaks. Zr is a much heavier atom and a larger change in the unit cell could be expected.

The SEM observations were consistent in that HEBM reduced the particle size from the "as bought" B_4C powder. The density of the samples showed that HEBM powder manufactured disks were very close to the “as bought” powder with no significant changes. The elemental inclusions with Si and Zr showed a reduced density compared to calculated TMD.

The high-impact shock experiments were conducted in two ways to measure the pressure achieved at the impact and the HEL of the ceramics. The Hugoniot pressure studies presented the impact pressures for both “as bought” and 1 atom Zr inclusion. Both tests were designed to compare the impact pressures at the same incident velocity but a lower velocity was observed for the “as bought” ceramic target.

The HEL experiments showed that the HEBM target behaved almost in the same way as the “as bought” one. The enriched samples with 1/2 Si and 1 Zr elemental inclusions showed a similar behavior regarding the HEL with the 1 atom Si elemental inclusions showing a greater reduced performance.

All five of the B_4C and B_4C variations showed post-yield hardening behavior after the HEL. But, the observed HELs were below the anticipated values.

Further studies should be performed to investigate the effects of hot-pressing and different ball milling processes to increase the HEL. In addition, a separate study on the exact location of the elemental inclusions should be performed using Extended X-ray Absorption Fine Structure (EXAFS) to uniquely determine the locations of the elemental inclusions from HEBM and what the alterations to the original B_4C unit cell from HEBM and elemental inclusions.

APPENDIX: Sample Data

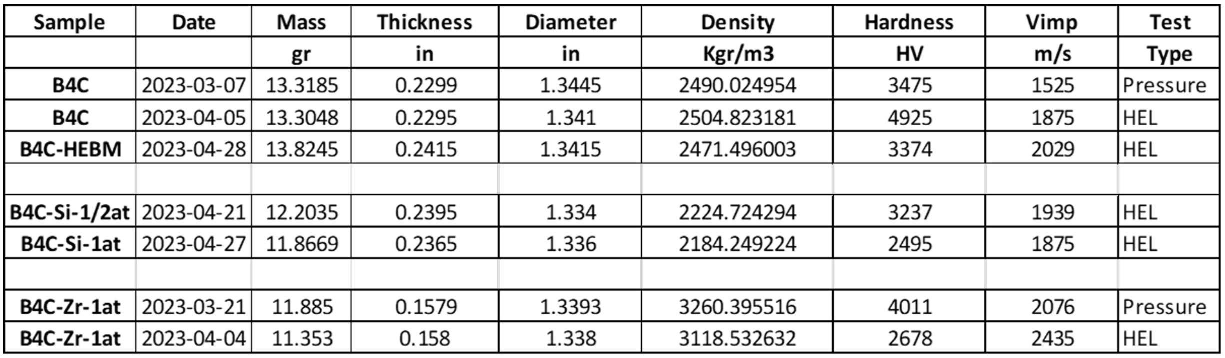

Sample	Date	Mass	Thickness	Diameter	Density	Hardness	Vimp	Test
		gr	in	in	Kgr/m3	HV	m/s	Type
B4C	2023-03-07	13.3185	0.2299	1.3445	2490.024954	3475	1525	Pressure
B4C	2023-04-05	13.3048	0.2295	1.341	2504.823181	4925	1875	HEL
B4C-HEBM	2023-04-28	13.8245	0.2415	1.3415	2471.496003	3374	2029	HEL
B4C-Si-1/2at	2023-04-21	12.2035	0.2395	1.334	2224.724294	3237	1939	HEL
B4C-Si-1at	2023-04-27	11.8669	0.2365	1.336	2184.249224	2495	1875	HEL
B4C-Zr-1at	2023-03-21	11.885	0.1579	1.3393	3260.395516	4011	2076	Pressure
B4C-Zr-1at	2023-04-04	11.353	0.158	1.338	3118.532632	2678	2435	HEL

Figure A.1. Sample Data

THIS PAGE INTENTIONALLY LEFT BLANK

List of References

[1] V. Tan, C. Lim, and C. Cheong, “Perforation of High-Strength Fabric by Projectiles of Different Geometry,” *International Journal of Impact Engineering*, vol. 28, no. 2, pp. 207–222, 2003. Available: https://www.sciencedirect.com/science/article/pii/S0734743X02000556

[2] S. Walley, “Historical Review of High-Strain Rate and Shock Properties of Ceramics Relevant to their Application in Armour,” *Advances in Applied Ceramics*, vol. 109, no. 8, pp. 446–466, 2010.

[3] W. A. Gooch, “An Overview of Ceramic Armor Applications,” *Ceramic transactions*, vol. 134, pp. 3–21, 2002.

[4] M. Wilkins, C. Cline, and C. Honodel, “Fourth Progress Report of Light Armor Program.” California Univ., Livermore. Lawrence Radiation Lab., Tech. Rep., 1969.

[5] “Nij Armor Protection Levels,” Understanding NIJ 0101.06 Armor Protection Levels. Available: https://www.ojp.gov/pdffiles1/nij/nlectc/250144.pdf

[6] P. Gautam, R. Gupta, A. Sharma, and M. Singh, “Determination of Hugoniot Elastic Limit (HEL) and Equation of State (EOS) of Ceramic Materials in the Pressure Region 20 GPa to 100 GPa,” *Procedia Engineering*, vol. 173, pp. 198–205, 2017, plasticity and Impact Mechanics. Available: https://www.sciencedirect.com/science/article/pii/S1877705816344496

[7] D. Grady, “Shock-Wave Strength Properties of Boron Carbide and Silicon Carbide.” *Le Journal de Physique IV*, vol. 4, no. C8, pp. C8–385, 1994.

[8] M. K. Kolel-Veetil, R. M. Gamache, N. Bernstein, R. Goswami, S. B. Qadri, K. P. Fears, J. B. Miller, E. R. Glaser, and T. M. Keller, “Substitution of Silicon within the Rhombohedral Boron Carbide (B4C) Crystal Lattice through High-Energy Ball Milling,” *Journal of Materials Chemistry C*, vol. 3, no. 44, pp. 11 705–11 716, 2015.

[9] V. Domnich, S. Reynaud, R. A. Haber, and M. Chhowalla, “Boron Carbide: Structure, Properties, and Stability under Stress,” *Journal of the American Ceramic Society*, vol. 94, no. 11, pp. 3605–3628, 2011.

[10] K. Shirai, “Electronic Structures and Mechanical Properties of Boron and Boron-Rich Crystals (Part i),” *Journal of Superhard Materials*, vol. 32, pp. 205–225, 2010.

[11] K. Shirai, "Electronic Structures and Mechanical Properties of Boron and Boron-Rich Crystals (Part 2)," *Journal of Superhard Materials*, vol. 5, no. 32, pp. 336–345, 2010.

[12] W. Gust and E. Royce, "Dynamic Yield Strengths of B4C, BeO, and Al2O3 Ceramics," *Journal of Applied Physics*, vol. 42, no. 1, pp. 276–295, 1971.

[13] D. Ge, V. Domnich, T. Juliano, E. Stach, and Y. Gogotsi, "Structural Damage in Boron Carbide under Contact Loading," *Acta Materialia*, vol. 52, no. 13, pp. 3921–3927, 2004.

[14] N. Bourne, "Shock-Induced Brittle Failure of Boron Carbide," *Proceedings of the Royal Society of London. Series A: Mathematical, Physical and Engineering Sciences*, vol. 458, no. 2024, pp. 1999–2006, 2002.

[15] D. Grady, "Shock-Wave Compression of Brittle Solids," *Mechanics of Materials*, vol. 29, no. 3-4, pp. 181–203, 1998.

[16] T. Vogler, W. Reinhart, and L. Chhabildas, "Dynamic Behavior of Boron Carbide," *Journal of applied physics*, vol. 95, no. 8, pp. 4173–4183, 2004.

[17] M. Chen and J. W. McCauley, "Mechanical Scratching Induced Phase Transitions and Reactions of Boron Carbide," *Journal of applied physics*, vol. 100, no. 12, p. 123517, 2006.

[18] G. Fanchini, J. W. McCauley, and M. Chhowalla, "Behavior of Disordered Boron Carbide under Stress," *Physical review letters*, vol. 97, no. 3, p. 035502, 2006.

[19] A. K. Chattopadhyay, O. Yilmaz, M. Bilen, and M. Baris, "Strengthening Boron Carbide and Prevention of High-Pressure Amorphization by Inducing Metals or Metal Borides across the Grain Boundary During Hot-Pressing or Sintering," *Adv. Powder. Metall. Part. Mater*, vol. 7, pp. 1–12, 2015.

[20] A. K. Chattopadhyay, "Selective Migration of Metals and Metal Borides to Strengthen Boron Carbide," *Metal Powder Report*, vol. 71, no. 2, pp. 106–111, 2016. Available: https://www.sciencedirect.com/science/article/pii/S002606571600151X

[21] A. Zolriasatein, A. Shokuhfar, F. Safari, and N. Abdi, "Comparative Study of SPEX and Planetary Milling Methods for the Fabrication of Complex Metallic Alloy Nanoparticles," *Micro & Nano Letters*, vol. 13, no. 4, pp. 448–451, 2018.

[22] M. V. Zelinkskas, "Improving the Material Properties of Boron Carbide Through Elemental Inclusion," Naval Postgraduate School, Tech. Rep., 2020.

[23] C. L. DeCastro and B. S. Mitchell, “Nanoparticles from Mechanical Attrition,” *Synthesis, Functionalization, and Surface Treatment of Nanoparticles*, vol. 5, 2002.

[24] L. Liu, S. Lun, S.-E. Liu, X.-D. Zhao, B. Yao, and W.-H. Su, “Thermodynamic Mechanisms of Mechanical Crystallization of Amorphous Fe-N Alloy,” *Journal of Alloys and Compounds*, vol. 333, no. 1-2, pp. 202–206, 2002.

[25] N. Hlabangana, G. Danha, and E. Muzenda, “Effect of Ball and Feed Particle Size Distribution on the Milling Efficiency of a Ball Mill: An Attainable Region Approach,” *South African Journal of Chemical Engineering*, vol. 25, pp. 79–84, 2018. Available: https://www.sciencedirect.com/science/article/pii/S1026918517300720

[26] T. D. Beaudet, J. R. Smith, and J. W. Adams, “Surface Energy and Relaxation in Boron Carbide (1011) from First Principles,” *Solid State Communications*, vol. 219, pp. 43–47, 2015.

[27] L. S. H. Data and S. Marsh, “Los Alamos Series on Dynamic Material Properties,” 1980.

[28] J. P. de Villiers and P. R. Buseck, “Mineralogy and Instrumentation,” in *Encyclopedia of Physical Science and Technology (Third Edition)*, R. A. Meyers, Ed., third edition ed. New York: Academic Press, 2003, pp. 1–27. Available: https://www.sciencedirect.com/science/article/pii/B0122274105004518

[29] “Scanning Electron Microscope,” *Wikipedia*. Accessed May 9, 2023 [Online]. Available: https://en.wikipedia.org/wiki/Scanning_electron_microscope

[30] “Vickers Hardness Test,” *Wikipedia*. Accessed April 10, 2023 [Online]. Available: https://en.wikipedia.org/wiki/Vickers_hardness_test

[31] “Weapons’ Physics,” class notes for Weapon Physics by Joe Hooper, Dept. of Physics, Naval Postgraduate School, Monterey, CA, USA, spring 2022.

[32] Q. Liu, X. Zhou, X. Zeng, and S. Luo, “Sound Velocity, Equation of State, Temperature and Melting of LiF Single Crystals under Shock Compression,” *Journal of Applied Physics*, vol. 117, no. 4, p. 045901, 2015.

THIS PAGE INTENTIONALLY LEFT BLANK

Initial Distribution List

1. Defense Technical Information Center
   Ft. Belvoir, Virginia

2. Dudley Knox Library
   Naval Postgraduate School
   Monterey, California